Exploring mechanisms responsible for tidal modulation in flow of the Filchner-Ronne Ice Shelf

Sebastian H. R. Rosier [1] and G. Hilmar Gudmundsson [1]

[1]Department of Geography and Environmental Sciences, Northumbria University, Newcastle upon Tyne, NE1 8ST, UK

Correspondence: S. Rosier (sebastian.rosier@northumbria.ac.uk)

Abstract. An extensive network of GPS sites on the Filchner-Ronne Ice Shelf and adjoining ice streams shows strong tidal modulation of horizontal ice flow at a range of frequencies. A particularly strong (horizontal) response is found at the fortnightly (M_{sf}) frequency. Since this tidal constituent is absent in the (vertical) tidal forcing, this observation implies the action of some nonlinear mechanism. Another striking aspect is the strong amplitude of the flow perturbation, causing a periodic reversal in the direction of ice-shelf flow in some areas, and a 10-20% change in speed at grounding lines. No model has yet been able to reproduce the quantitative aspects of the observed tidal modulation across the entire Filchner-Ronne Ice Shelf. The cause of the tidal ice flow response has therefore remained an enigma, indicating a serious limitation in our current understanding of the mechanics of large-scale ice flow. A further limitation of previous studies is that they have all focused on isolated regions and interactions between different areas have, therefore, not been fully accounted for. Here, we conduct the first large-scale ice-flow modelling study to explore these processes using a viscoelastic rheology and realistic geometry of the entire Filchner-Ronne Ice Shelf, where the best observations of tidal response are available. We evaluate all relevant mechanisms that have hitherto been put forward to explain how tides might affect ice-shelf flow and compare our results with observational data. We conclude that, while some are able to generate the correct general qualitative aspects of the tidally-induced perturbations in ice flow, most of these mechanisms must be ruled out as being the primary cause of the observed long-periodic response. We find that only tidally-induced lateral migration of grounding lines can generate a sufficiently strong long-periodic M_{sf} response on the ice shelf to match observations. Furthermore, we show that the observed horizontal short-periodic semidiurnal tidal motion, causing twice-daily flow reversals at the ice front, can be generated through a purely elastic response to basin-wide tidal perturbations in the ice shelf slope. This model also allows us to quantify the effect of tides on mean ice flow and we find that the Filchner-Ronne Ice Shelf flows, on average, $\sim$21% faster than it would in the absence of large ocean tides.

1 Introduction

Much of the Antarctic Ice Sheet is surrounded by floating ice shelves, and early research suggested that these ice shelves may have a significant mechanical impact on upstream flow (Thomas, 1973; Hughes, 1973). More recently, observations following ice shelf disintegration and modelling efforts have confirmed this 'buttressing' effect and enabled a quantification of its importance (Rott et al., 2002; De Angelis and Skvarca, 2003; Rignot et al., 2004; Furst et al., 2018; Reese et al., 2018). Ice shelves are now thought to modify upstream flow and to impact the stability regime of grounding lines (Gudmundsson,

2013; Pegler, 2018; Haseloff and Sergienko, 2018). Understanding the mechanics of ice-shelf flow is therefore of considerable importance for assessing the future evolution of ice discharge from the ice sheet's interior, across grounding lines, and into the ocean.

Recently, an increasing quantity of GPS and InSAR observations have revealed that the flow of both ice shelves and ice streams can be strongly modulated by ocean tides, leading to substantial temporal variations in velocity (Riedel et al., 1999; Doake et al., 2002; Legresy et al., 2004; Brunt et al., 2010; King et al., 2011; Alley, 1997; Bindschadler et al., 2003; Anandakrishnan et al., 2003; Gudmundsson, 2006; Marsh et al., 2013; Minchew et al., 2016; Rosier et al., 2017a). The existence of tidal effects in ice-shelf flow is not surprising in and of itself, but the strength and nature of these tidal effects is in many cases both striking and unexpected. Firstly, the horizontal response of the Filchner-Ronne ice shelf is strongest at a tidal frequency not found in the vertical tides that force it. As we discuss in more detail below, while the primary (vertical) ocean tidal constituents are the semidiurnal (M_2, S_2) and the diurnal (K_1, O_1) frequencies, the single largest (horizontal) ice-shelf tidal constituent is the M_{sf} tide with a period of 14.76 days (Rosier et al., 2017a). This M_{sf} constituent is absent in the vertical ocean tides beneath the ice shelf, an observation that implies the existence of some nonlinear mechanism capable of transferring tidal energy from short (M_2, S_2, O_1, K_1) to long (M_{sf}) periods. If the response were purely a linear function of the vertical tidal forcing, no new frequencies could be generated. Secondly, the observed tidal flow perturbations are much stronger and more widespread than one might have expected based on models that only include elastic flexure (e.g. Rack et al., 2017). The long-periodic response gives rise to 5 to 20 % changes in flow velocities across the whole ice shelf. Hence, these modulations in flow are not limited to the elastic flexure zone in the grounding zone. Finally, the shorter period tidal response can give rise to even larger changes in ice-shelf velocity due to their higher frequency. In some locations the tidal modulation is strong enough to cause a periodic reversal in ice flow direction (Makinson et al., 2012).

The range of timescales over which tidal effects are seen to operate suggests that studying these processes may yield insights into both the elastic and viscous properties of ice, thereby providing an opportunity to constrain ice rheology over spatial and temporal scales of direct relevance to ice sheet models. Furthermore, the mechanical coupling between vertical ocean tides and ice flow through ice flexure occurs in the grounding zone, a particularly important and complex part of the ice sheet where our modelling and observational efforts are often focused. Given both the complexity of this behaviour and the difficulties in reproducing it, modelling these processes can be viewed as a test of our understanding of how ice flows across grounding lines and through ice shelves to the ocean.

Previously, Brunt and MacAyeal (2014) studied the tidal response of the Ross Ice Shelf using a viscous model. While the assumption of viscous rheology appears justified for studies of secular ice flow, this assumption is not appropriate for a study of processes at tidal timescales where viscoelastic effects can be expected to play a significant role in the deformation of ice (Jellinek and Brill, 1956). In this paper, we use a full-Stokes three-dimensional (3D) viscoelastic model to investigate the causes of the observed horizontal tidal modulation of ice flow over Filchner-Ronne Ice Shelf. Our particular focus will be to investigate possible causes for both the strong semidiurnal modulation of ice-shelf flow at the M_2 frequency together with the fortnightly modulation at the M_{sf} frequency whose origin is much debated (Gudmundsson, 2007, 2011; Thompson et al., 2014; Rosier et al., 2014, 2015; Minchew et al., 2016; Robel et al., 2017; Rosier and Gudmundsson, 2018). The model domain

includes the entire Filchner-Ronne Ice Shelf and we test all the mechanisms (as summarised below) that have been suggested in previous studies as responsible for generating the observed tidal response of the ice shelf.

The paper is structured as follows: We begin by giving a background to ocean tides in the study area and an overview of observations showing tidal modulation of ice-shelf flow, followed by a summary of previous attempts at explaining these observations. We then present our numerical model and key results. Most of the detailed technical descriptions related the numerical experiments and implementations of different physical processes are found in several separate appendices. We find that many of the previously proposed explanations, while capable of producing a response at the correct frequencies, cannot generate a nonlinear response with a sufficiently large amplitude to match observations. Our proposed explanation, partly arrived by process of elimination, is that the tidal effects must to a large extent be caused by a tidally induced migration of grounding lines coupled with the nonlinear rheological response of ice.

1.1 Ocean tides beneath the Filchner-Ronne Ice Shelf

Tidal models constrained by GPS observations have lead to accurate knowledge of vertical tidal motion beneath the Filchner-Ronne Ice Shelf Padman et al. (2002). Vertical tides at the grounding lines of ice streams feeding into the Ronne Ice Shelf are the largest in Antarctica, with a tidal range of up to 8 m (Fig. 1, dashed contours), making this an ideal location to investigate tidal effects on ice-shelf flow.

Vertical tidal motion can be split into many tidal constituents, each with a unique period. Of these constituents, the semidiurnal M_2 (principal lunar) and S_2 (principal solar) constituents have the largest amplitudes in this region. They are characterized by an amphidromic point, where their amplitude is zero and around which they rotate, located near the centre of the Ronne Ice Shelf front. These two constituents have periods of approximately 12.42 and 12 hours, respectively, and their combined wave envelope gives rise to the spring neap tidal cycle. This wave envelope should not be confused with the M_{sf} frequency, despite having the same apparent 'period' of 14.76 days. The M_{sf} frequency is found in spectral analysis of horizontal ice shelf and ice stream displacements, but not in the vertical tidal motion, since the semidiurnal wave envelope contains no energy at a fortnightly period. In addition to the important semidiurnal constituents, two diurnal constituents (O_1 and K_1) also have relatively large amplitudes, increasing near the grounding lines. Unlike the semidiurnal constituents, these do not rotate around an amphidromic point, and instead their phase increases approximately linearly through the region, from east to west.

1.2 Observations of tidally modulated horizontal ice-shelf displacement

The first GPS observations to find tidal modulation of horizontal ice-shelf flow were made in the Ekström Ice Shelf grounding zone (Riedel et al., 1999). In the years since, similar observations have been made on the Brunt (Doake et al., 2002; Gudmundsson et al., 2017), Ross (Brunt et al., 2010), Larsen C (King et al., 2011) and Filchner-Ronne ice shelves (Makinson et al., 2012; Rosier et al., 2017a) and the Mertz glacier tongue (Legresy et al., 2004). In terms of ice shelf velocities, different tidal constituents dominate depending on the local tidal regime. For example in the Ross sea the diurnal constituents (O_1 and K_1) dominate the vertical ocean tidal signal and the (horizontal) ice-shelf flow response. Conversely, in the Weddell Sea, the semidiurnal constituents are strongest in both the vertical (Sec. 1.1) and horizontal motion (Makinson et al., 2012).
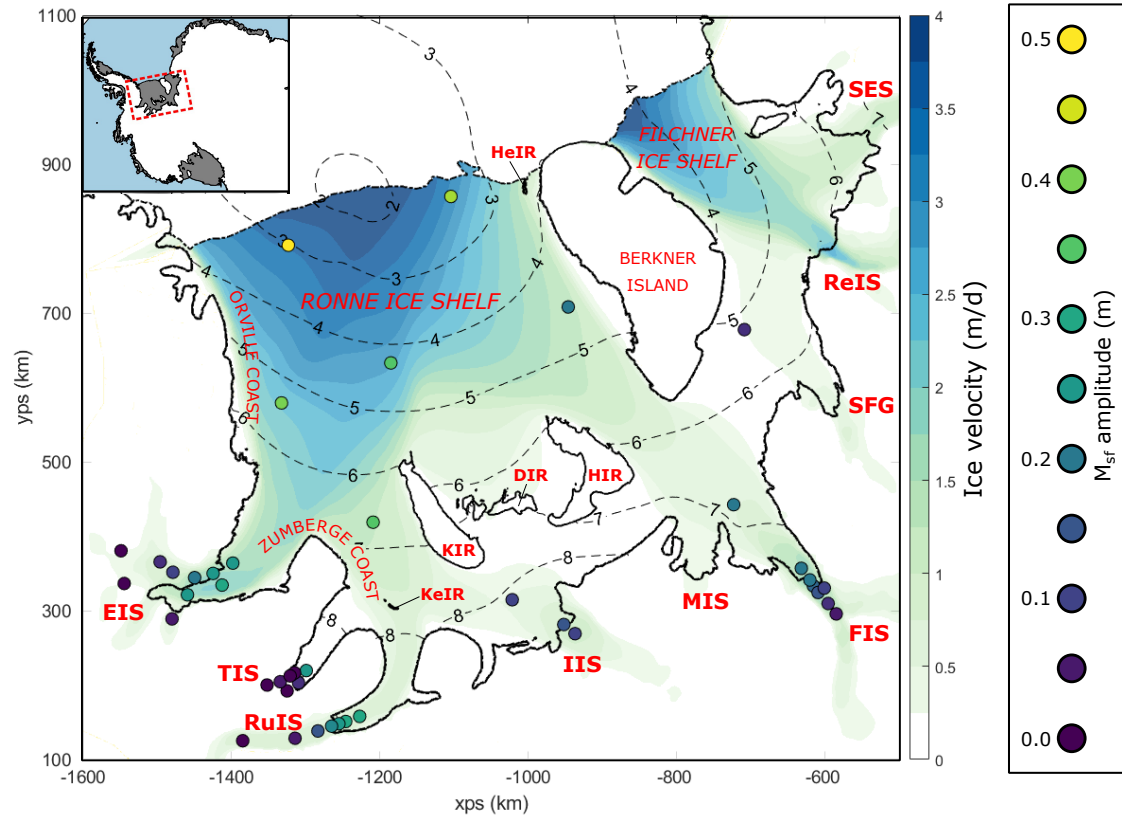
Figure 1. Map showing the Filchner-Ronne Ice Shelf and adjoining ice streams. Circular markers show locations of GPS sites and are coloured according to M_{sf} amplitude. The background colourmap shows ice speed, grounding lines are indicated by solid black lines, dashed contour lines show tidal range (in meters) and solid gray contour lines show ice surface elevation. Acronyms for glaciological features marked on the map are as follows: Evans Ice Stream (EIS), Talutis Ice Stream (TIS), Rutford Ice Stream (RuIS), Institute Ice Stream (IIS), Moller Ice Stream (MIS), Foundation Ice Stream (FIS), Support Force Glacier (SFG), Recovery Ice Stream (ReIS), Slessor Ice Stream (SES), Hemmen Ice Rise (HeIR), Korff Ice Rise (KIR), Kershaw Ice Rumples (KeIR), Doake Ice Rumples (DIR) and Henry Ice Rise (HIR).

In this study, we focus our modelling efforts on the Filchner-Ronne Ice Shelf where we have a relatively large number of observations and the largest (vertical) ocean tidal amplitudes in the whole of Antarctica. A network of nine GPS stations made measurements spanning over a year in locations both near the Ronne ice front and further into the shelf (Makinson et al., 2012). These GPS measurements reveal strong horizontal tidal modulation at diurnal and semidiurnal frequencies. During the spring tide, at sites near the ice front, horizontal velocity and strain varied by $\pm300\%$ of the mean values over a tidal cycle, periodically causing direction of flow to be reversed (Makinson et al., 2012). Further upstream from the calving front, horizontal diurnal and semidiurnal signals were found to decay to almost zero.

A more recent study, that included several additional GPS sites deployed for up to a year near the outlet of major ice streams feeding the Ronne Ice Shelf, found that the response over semidiurnal and diurnal periods increased again towards

the grounding lines (Rosier et al., 2017a). Further analysis of all available GPS data also revealed a strong M_{sf} component in horizontal ice shelf displacements across the entire floating ice shelf (Rosier et al., 2017a). This signal had previously been found on grounded ice streams (Gudmundsson, 2006; Minchew et al., 2016) and at a few locations on the Larsen C and Brunt Ice Shelves (King et al., 2011; Gudmundsson et al., 2017) but has now been found to occur over a vast area and with an amplitude typically greater than had been found on ice streams (Rosier et al., 2017a).

1.3 Proposed mechanisms for tidal modulation of ice-shelf flow

With the realisation that tides can strongly modulate ice flow, many different mechanisms have been put forward to explain these observations. Initially, Doake et al. (2002) suggested that currents beneath the Brunt Ice Shelf could be responsible for the tidal signals found there and this idea was explored further by Legresy et al. (2004) and Brunt and MacAyeal (2014). More recently, the discovery of an M_{sf} signal far upstream of the RuIS (Rutford Ice Stream) grounding line (Gudmundsson, 2006) has lead to a focus on replicating these observations (Gudmundsson, 2007, 2011; Rosier et al., 2014, 2015; Minchew et al., 2016) and much less has been done to understand the origin of horizontal tidal signals on ice shelves.

The large horizontal semidiurnal modulation of the Filchner-Ronne Ice Shelf flow was discovered by Makinson et al. (2012), who suggested that it could be explained by an elastic response to tilting of the ice shelf as tides rotate around the amphidromic point. On the Ross Ice Shelf, Brunt and MacAyeal (2014) used a purely viscous model to explore the effects of both tilt and currents but found that they could not replicate GPS observations. Neither of these studies investigated longer period modulation of ice-shelf flow.

Efforts to understand the cause of the long period M_{sf} signal, now known to occur across many of the large West Antarctic Ice Shelves where we have GPS data, require a nonlinear mechanism (Gudmundsson, 2007). The paucity of observations of this type on ice shelves led for some time to an implicit assumption that any M_{sf} signal observed on ice shelves was transmitted directly from grounded ice rather than generated in floating regions. The increasing number of observations of the M_{sf} signal, revealing that in at least some cases the phase leads and amplitude is greatest downstream of grounding lines, have made it clear that additional mechanisms must be at play (Minchew et al., 2016; Rosier et al., 2017a).

One possible nonlinear mechanism is that vertical tidal motion causes the grounding line to migrate back and forth sufficiently far as to have an effect on ice flow. Evidence of tidal migration of grounding lines remains relatively sparse but measurements of this process have been inferred via remote sensing (Schmeltz et al., 2001; Brunt et al., 2011; Milillo et al., 2017) and cryoseismicity (Pirli et al., 2018). This could give rise to several nonlinearities: firstly this can result in the width of the ice shelf changing as the portion of floating ice changes over one tidal cycle (Minchew et al., 2016). In addition, the grounding line migration may be assymetric (Tsai and Gudmundsson, 2015) resulting in a greater migration upstream during high tide than downstream during low tide (Rosier et al., 2014). Another consequence of tidally induced grounding line migration was explored by Robel et al. (2017), who suggested that changes in buttressing arising from grounding line migration could explain observations on RuIS.

An alternative mechanism, termed "flexural ice softening", that results directly from the nonlinear rheology of ice itself, was put forward by Rosier and Gudmundsson (2018). The authors showed that tidal bending stresses in the grounding zone, which

Table 1. Overview of the various model versions, including a brief description of how each one differs from the 'default setup' and the relevant appendix in which more details can be found.

Model version name	Description	Appendix no.
Default setup	The default model setup, as described in the methods	N/A
RF_n5	Uses an exponent of 5 in Glen's flow law	Appendix A
RF_n4	Uses an exponent of 4 in Glen's flow law	Appendix A
RF_Anoreg	Uses a rate factor of ice with no regularisation	Appendix A
RF_streams	Includes grounded ice streams in the domain	Appendix B
RF_damage	Includes damage effects in the ice rheology	Appendix C
RF_burgers	Uses a Burgers rheological model for ice	Appendix D
RF_GLmigration	Includes a parameterization of GL migration along model sidewalls	Appendix E
RF_currents	Includes sub ice shelf tidal current drag stresses	Appendix F
RF_temperature	Includes the effects of ice temperature on the rate factor of ice	Appendix G
RF_thinGZ	Reduces the thickness of ice in the grounding zone	Appendix H

will vary in magnitude over a tidal cycle, could lead to a sufficiently large change in the effective viscosity of ice in this region such that ice flow would be enhanced at high and low tide and lead to modulation of ice-shelf flow at the M_{sf} frequency. Each of these nonlinear mechanisms could be playing a role in generating the observed M_{sf} signal.

Our main objective in this paper is to narrow down the possible causes of observed tidal motion of the Filchner-Ronne ice shelf by quantifying the contributions of several different processes using a 3D viscoelastic model and comparing these results with observations. In particular we will focus on modelling the two strongest responses observed in horizontal ice-shelf flow: at the M_2 and M_{sf} frequencies.

2 Methods

In this section, we present a description of the 3D full-Stokes viscoelastic model used to investigate tidal modulation of ice-shelf flow. What is described below is what we call the 'default setup'. Several model experiments necessitated modifications or additional features to this setup and these differences are stated explicitly below. The various model versions that arise due to these differences are listed in Table 1 and each is explained in more detail in the relevant appendix.

2.1 Field equations

We use a 3D full-Stokes viscoelastic model in a Lagrangian frame of reference to solve for conservation of mass, linear momentum and angular momentum (respectively):

$$\frac{D\rho}{Dt} + \rho v_{i,i} = 0,$$ (1)

$$\sigma_{ij,j} + f_i = 0,$$ (2)

$$\sigma_{ij} - \sigma_{ji} = 0,$$ (3)

using the commercial finite element analysis software MSC.Marc (MSC, 2017). In the equations listed above, D/Dt is the material time derivative, v_i are the components of velocity, σ_{ij} are the components of the stress tensor, ρ is the ice density and f_i are the components of the gravity force. We use commas to denote partial derivatives with respect to the spatial coordinates and the summation convention for indices.

Ice rheology is represented by an upper-convected Maxwell model that relates deviatoric stresses τ_{ij} and deviatoric strains e_{ij} with

$$\dot{e}_{ij} = \frac{1}{2G}\overset{\triangledown}{\tau}_{ij} + A\tau_E^{n-1}\tau_{ij},$$ (4)

where A is the rate factor, $\tau_E = \sqrt{\tau_{ij}\tau_{ji}/2}$ is the effective stress, n is the constant in Glen's flow law, G is the shear modulus

$$G = \frac{E}{2(1+\nu)},$$ (5)

ν is the Poisson's ratio and E is the Young's modulus (Shames and Cozzarelli, 1997). The superscript $\triangledown$ denotes the upper-convected time derivative, i.e.

$$\overset{\triangledown}{\tau} = \partial_t \tau + v \cdot \nabla \tau - (\nabla v)^T \cdot \tau - \tau \cdot \nabla v,$$ (6)

and deviatoric stresses and strains are defined by

$$e_{ij} = \epsilon_{ij} - \frac{1}{3}\delta_{ij}\epsilon_{kk}$$ (7)

and

$$\tau_{ij} = \sigma_{ij} - \frac{1}{3}\delta_{ij}\sigma_{kk}$$ (8)

respectively, where ϵ_{ij} are the components of the strain tensor. In all simulations we use a value for the Poisson's ratio of 0.41 in line with previous studies (Gudmundsson, 2011; Rosier et al., 2014, 2017a) and this choice has no effect on our

results. The rate factor is inverted for via the adjoint method implemented in the Úa ice-flow model (Gudmundsson et al., 2012) to match observed surface ice velocities (Rignot et al., 2017, 2011a; Mouginot et al., 2012), as outlined in Appendix A, and the resulting velocity field is shown in Fig. 2c. A table outlining the model parameter choices for the 'default setup' is shown in 2. The rheology outlined above is modified in three of the experiments. The RF_Burgers experiment uses a Burgers

5   rheology (Appendix D), the RF_temperature experiment makes A a function of temperature (Appendix G) and the RF_damage experiment adds a damage term in the elastic component of the Maxwell rheology (Appendix C).

2.2   Boundary conditions

At the base of the ice shelf and along the ice front, a pressure is applied normal to the element faces given by

$$p = \begin{cases} \rho_w \, g(S(x,y,t) - z(t)) & \text{if } z(t) < 0 \\ 0 & \text{otherwise} \end{cases} \tag{9}$$

10   where ρ_w is the sea water density and $S(x,y,t)$ is the time varying local sea level (Sec. 2.3). At the ice surface, a stress-free boundary condition is imposed such that

$$\boldsymbol{\sigma} \cdot \mathbf{n} = 0 \tag{10}$$

where $\mathbf{n}$ is the unit vector normal to the boundary. The only other boundary condition (BC) necessary in this 'default setup' is along the grounded sidewalls of the ice shelf domain. A Dirichlet BC is imposed on nodes along the grounded edge of the

15   model, such that

$$u = u_{obs} \qquad\qquad v = v_{obs} \qquad\qquad w = 0 \tag{11}$$

where u_{obs} and v_{obs} are observed surface velocities (Rignot et al., 2017, 2011a; Mouginot et al., 2012) and constant in time. This BC allows for in-flow from fast moving ice streams but clamps nodes vertically at the grounding line such that ice in the grounding zone must bend to accommodate vertical tidal motion of the ice shelf. Another result of using this Dirichlet

20   BC is that the GL cannot migrate in these simulations, however later we will introduce a different model setup in which this constraint is loosened. We use Bedmap2 (Fretwell et al., 2013) to define the model geometry; including ice thickness, ice surface elevation and grounding line position.

2.3   Tidal forcing

We use the circum-Antarctic inverse model (referred to hereafter as CATS2008a, which is an updated version of the inverse

25   tidal model described by Padman et al. (2002)), to force our viscoelastic model at the ocean boundary with vertical tidal motion. By most measures, CATS2008a remains the best performing tidal model in this region (King et al., 2011). The CATS2008a model includes ten tidal constituents and we opt to force our model with the four largest constituents in the region by amplitude (M_2, S_2, O_1 and K_1), representing the principal semidiurnal and diurnal constituents. With these four constituents the most

Table 2. List of model parameter choices for the default model setup.

Parameter	Value	Unit
ρ_w	1030	kg m^{-3}
g	9.81	m s^{-2}
n	3	-
ν	0.41	-
E	2.4×10^9	Pa

important tidal features are captured such as the spring neap cycle and the rotation of tides around Weddel Sea amphidromic point. The fortnightly M_{sf} signal is produced through interaction between the M_2 and S_2 constituents and we include the diurnal constituents to ensure that the total tidal range is close to what is observed. The advantage of forcing the model with only these four constituents is to ensure that any other tidal frequencies that arise in the model must be generated through internal processes rather than directly from the forcing. The tidal model domain uses a slightly different grounding line to that used in the model presented herein, particularly at the outlet to Evans Ice Stream, so interpolation is done to fill in areas with no amplitude or phase information in CATS2008a.

2.4 Element discretisation

The finite element mesh uses 3D, fifteen-node, isoparametric pentahedrons, arranged such that the triangular faces are orientated in the horizontal plane (Fig. 2b). The pentahedral shape is well suited to modelling an ice shelf in three dimensions, since the triangular faces enable the element to conform to a complicated coastline geometry without an excessive number of elements and the relatively flat surfaces of the ice shelf are captured well with the quadrilateral faces. The stiffness of the element is formed using 21-point Gaussian integration and triquadratic interpolation shape functions are used for displacements, resulting in a linear variation in stress through the element. The model mesh, generated using mesh2d (Engwirda, 2014), is unstructured and refined around grounding lines and in regions of high lateral shear strain (Fig. 2a). Certain model versions necessitate a different mesh but the total number of elements remains approximately the same and results in between 5×10^5 and 1×10^6 degrees of freedom.

To test the effects of mesh resolution on our model results we ran simulations in which horizontal and vertical mesh resolution were doubled. The main differences in modelled M_{sf} amplitude are confined to the grounding zone, with a maximum change in amplitude across all nodes of 1 cm. Over the bulk of the shelf, the difference in M_{sf} amplitude between the simulations was typically of order 1 mm or less. Similarly, differences in the horizontal M_2 signal were limited to the grounding zone, with higher resolution resulting in similar amplitudes but a more confined band of tidal motion at this frequency.
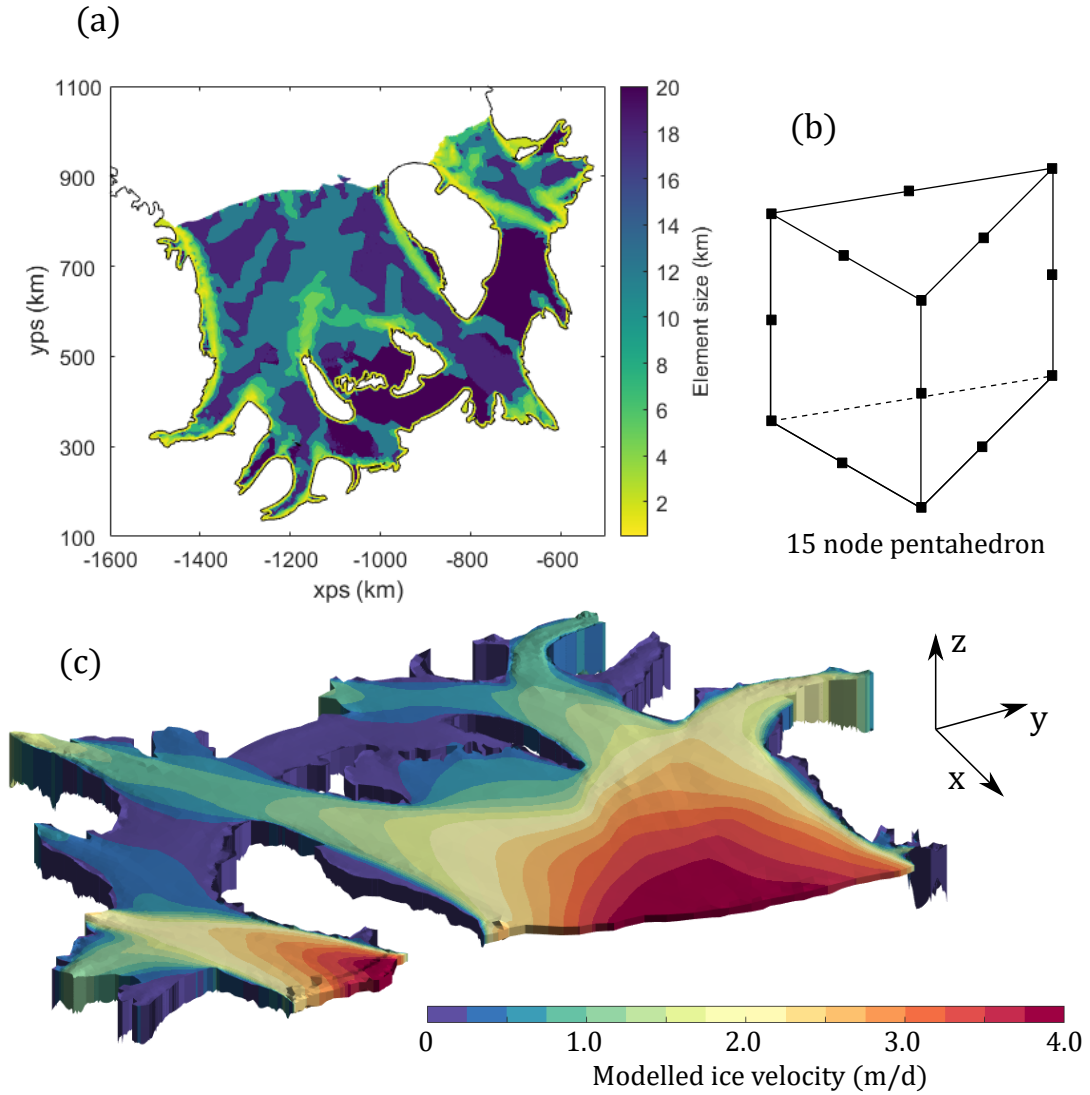
Figure 2. Overview of the finite element model, showing model resolution (panel a), the quadratic pentahedral elements used (panel b) and a vertically exaggerated oblique view of the model showing modelled mean ice velocity for the 'default setup' experiment (panel c).

3 Results

A number of different model setups were used in the course of this study. Our strategy, whose motivation will become clear later, was to begin by attempting to reproduce GPS observations of horizontal tidal displacements at the principal semidiurnal (M_2) frequency. Once the model was able to reproduce these observations we subsequently searched for the source of the fortnightly (M_{sf}) frequency by testing a number of mechanisms and parameter combinations. Our results are therefore structured in that
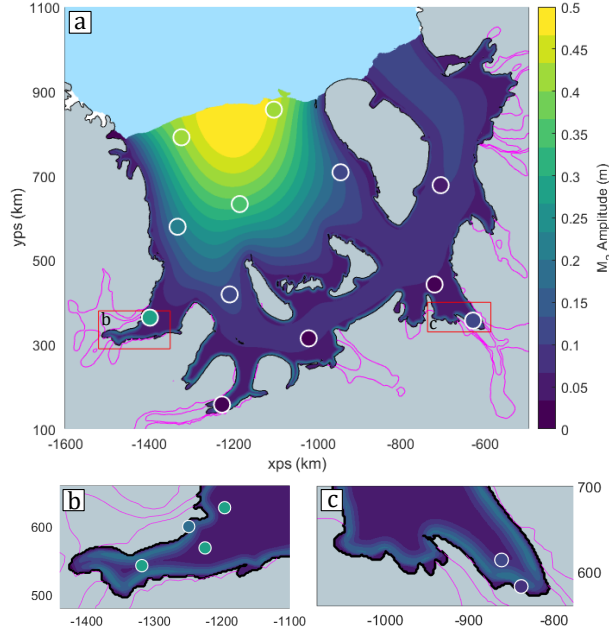
Figure 3. Amplitude of modelled horizontal ice shelf displacements at the M_2 frequency (background colourmap), compared with GPS observations (circles). Magenta lines are $0.5 \, \mathrm{m \, d^{-1}}$ ice velocity contours, to help identify regions of fast flowing grounded ice. Grounded ice is coloured gray, open ocean blue and ice shelves not included in the model domain are white.

order and we begin by presenting model results at the M_2 frequency. In all cases, the two horizontal components of modelled surface nodal displacements were processed using the Utide MATLAB package (Codiga, 2011). This state-of-the-art tidal analysis software calculates amplitudes of tidal constituents using an iteratively reweighted least squares method and our model results are largely presented in terms of the semi-major axis amplitude of each constituent.

3.1 Semidiurnal (M_2) results

Modelled horizontal ice shelf displacements at the M_2 frequency only differed slightly between all the model experiments set out in Table 1 and so we only present the M_2 results from the 'default setup'. A large amplitude M_2 component in modelled ice-shelf flow is found around most grounding lines and towards the ice shelf front (modelled M_2 amplitude is shown by the main colourmap in Fig. 3). The maximum in the modelled M_2 signal is focused around the M_2 amphidromic point, near the centre of the ice shelf front, where the amplitude approaches $0.5 \, \mathrm{m}$.

The difference between the modelled and observed response at the M_2 frequency is small over the majority of the ice shelf (GPS observations of M_2 amplitude are indicated by coloured circles in Fig. 3, using the same colour scale as the background colourmap). In particular, the bulk signal revealed by GPS observations of increasing amplitude towards the ice front is reproduced by the model. The only discrepancy occurs at GPS locations located near grounding lines but outside of the

immediate grounding zone. GPS observations at these locations reveal a stronger amplitude M_2 signal than that generated in the model, where it largely remains confined to the narrow grounding zone (Fig. 3). This mismatch is largest around the outlet of EIS, where modelled M_2 amplitude is ∼30% of the value measured by GPS. Any horizontal tidal motion must decay to zero at the grounding line as a result of our model BCs and so this mismatch is alleviated somewhat in experiments where this
5   constraint is removed (described later).

    A number of model experiments were conducted specifically to better understand the model response at the M_2 frequency. Firstly, the Young's modulus was both increased and decreased (between 1 and 9 GPa) to investigate how this affects the M_2 signal. This was found to only alter the amplitude of the M_2 effect and not its spatial variability; an increase in E reduced the amplitude and vice versa for a decrease in E. Since the modelled M_2 amplitude is only sensitive to E, we treat it as a tuneable
10   parameter and found that a value of $E = 2.4$ GPa produced a very good fit to observations.

    Two further model experiments were carried out to confirm the mechanisms responsible for generating this M_2 signal in the model. In the first, the vertical Dirichlet boundary condition imposed along the sides of the ice shelf was removed. In this experiment, the bulk M_2 signal across the majority of the shelf was identical but no M_2 signal was generated in the grounding zone since bending effects were removed. The second experiment set the amplitude and phase of all tidal constituents to be
15   the same in the whole domain (equal to the mean amplitude in this region). This stops the ice shelf from tilting due to spatial variation in either tidal amplitude or phase. With this setup the model only generates an M_2 signal in the grounding zone and there is no horizontal displacement at the M_2 frequency across the main bulk of the ice shelf. These two additional experiments hence confirm that the M_2 signal is primarily generated through ice-shelf tilting with a small localised component generated near grounding lines due to tidal flexure.

20   **3.2   Lunar synodic fortnightly (M_{sf}) results**

    Having identified the mechanism responsible for generating the M_2 signal and having selected an appropriate value for E we now turn our attention to the M_{sf} signal. A number of model experiments were conducted, including various different processes (as outlined in table 1) in an effort to determine possible sources of the observed fortnightly (M_{sf}) modulation in flow of the Filchner-Ronne Ice Shelf. These runs can broadly be split into two categories; those in which the flexural softening mechanism
25   is primarily responsible for generating an M_{sf} signal and those that allow the GL to move and in which tidally induced GL migration is the primary mechanism at play.

  3.2.1   Flexural softening experiments

    The strength of the M_{sf} signal generated through the flexural softening mechanism, as proposed by Rosier and Gudmundsson (2018), is sensitive to a number of different modelling choices. We explore whether any of these could yield an M_{sf} signal
30   similar to observations and the results of these model simulations are shown in Fig. 4. Firstly, the 'default_setup' experiment produces an M_{sf} response whose spatial distribution appears to agree reasonably well with GPS measurements but the amplitude is much smaller than observed (Fig. 4a). For example, towards the ice shelf front, where the M_{sf} signal has a measured amplitude of ∼0.5 m, the modelled M_{sf} amplitudes are about an order of magnitude smaller. Similarly poor numerical fit to
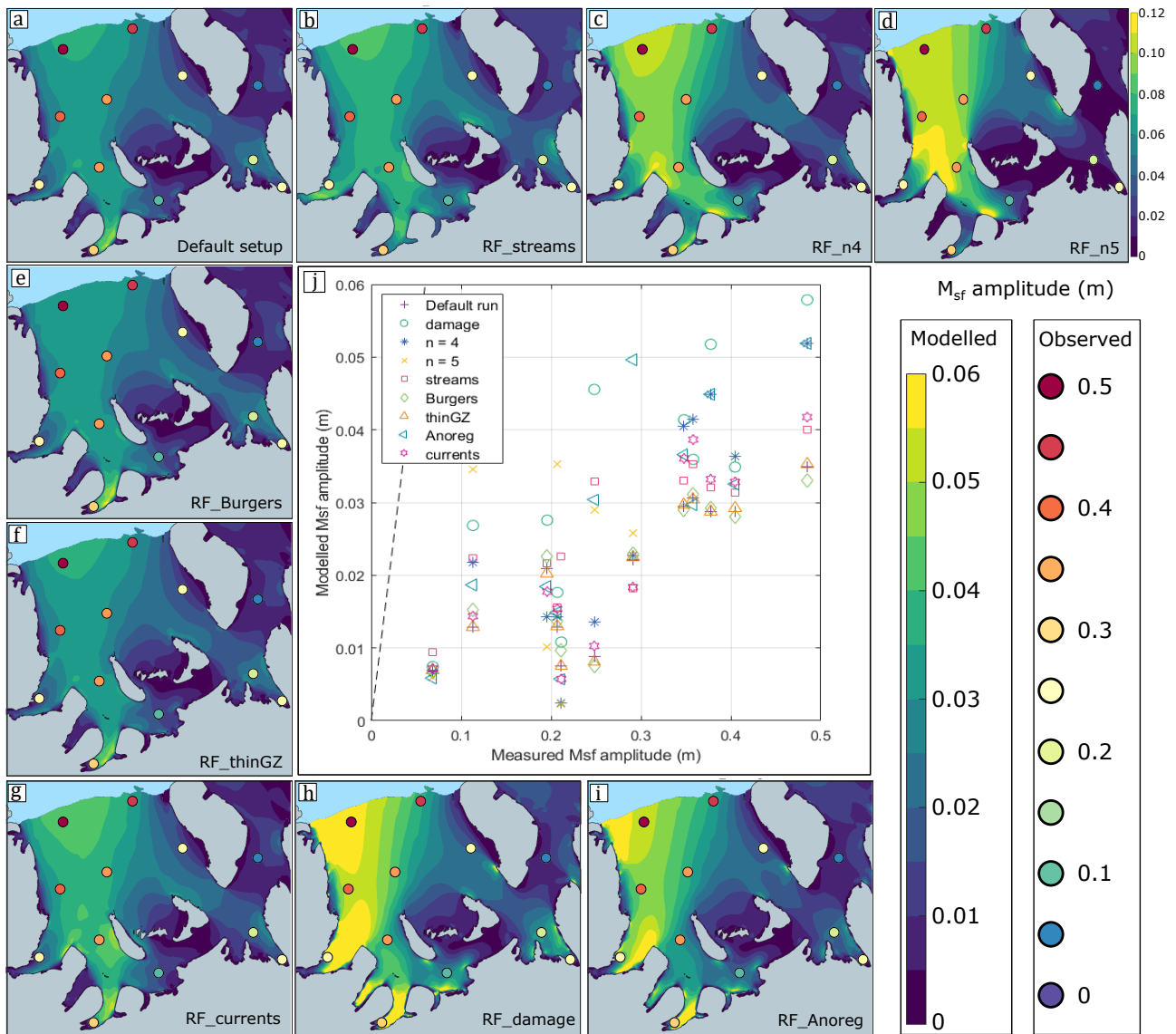
Figure 4. M_{sf} amplitude on the Ronne Ice Shelf for nine of the model experiments (panels a - i) outlined in table 1. Note the different colour scale used for experiment 'RF_n5' in panel d. Observed M_{sf} amplitudes from GPS observations are indicated in panel a by coloured circles. Panel j compares measured and modelled M_{sf} amplitude at each of the marked locations for the same set of experiments. Note that in producing this figure we use an evenly distributed subset of measurements to avoid bias in areas with more measurements and thus make interpretation of the overall misfit across the entire ice shelf easier.

observations is found around the grounding zones, where a large number of GPS observations exist. We thus conclude that although the 'default setup' produces a realistic looking spatial variation in Msf amplitudes, either the parameter values used

are incorrect, or some essential physics are missing. To identify the cause of the misfit we start by investigate the sensitivity of the modelled response to various parameter values.

Since it is the nonlinear aspect ice rheology that drives the flexural softening mechanism and gives rise to the non-linear Msf response we start my changing the value of the ice-flow stress exponent. Increasing the exponent in the Glen-Steinemann flow law from $n = 3$ to $n = 4$ (Fig. 4c) or $n = 5$ (Fig. 4d, note the different colour scale used for this panel) increases the M_{sf} amplitude substantially. However, not sufficiently to match observations. We tested the use of the more complex Burgers rheology, which includes the delayed elastic response (Appendix D), but this only lead to a 5-10% change in the M_{sf} amplitude compared to that of the 'default_setup' (Fig. 4e). We then tried several different spatial distributions of the rate factor A. For example in the 'RF_Anoreg' experiment we used a different rate factor field, as in the 'default setup' obtained through inversion of surface velocities using the ice-flow model Úa but this time without any regularisation (Appendix A). The resulting M_{sf} amplitude is generally larger than the 'default_setup', particularly along Western margins in the domain with a high spatial heterogeneity in the rate factor field where modelled M_{sf} amplitudes are increased by ~50%, but still much smaller than observations (Fig. 4i). Thus, despite changing the value of the ice-flow stress exponent n, changing the distribution of the rate factor A, and using an alternative rheological model, we were not able to match the observed Msf amplitudes.

The geometry used in the 'default_setup' model assumes hydrostatic equilibrium to calculate ice shelf thickness from known surface elevation, but this assumption breaks down near grounding lines where bridging stresses become important. Since the bending stresses that generate an M_{sf} signal in the 'default_setup' are sensitive to ice thickness in the grounding zone we conduct the 'RF_thinGZ' experiment in which ice thickness is reduced in this region, as outlined in Appendix H. This change in geometry only has a small impact on the overall M_{sf} amplitude (Fig. 4f). Crevassing in the grounding zone could also reduce the effective stiffness of ice and thereby alter the magnitude of tidal bending stresses. In the 'RF_damage' model experiment we adopt a continuum damage mechanics approach to simulate this effect (Appendix C). This experiment has a more profound effect on effective ice stiffness and thus leads to larger changes in the M_{sf} amplitude (Fig. 4h) but once again these are too small to match observations.

Various authors have suggested that sub ice shelf tidal currents could play a role in modulating horizontal ice velocities at tidal frequencies (Doake et al., 2002; Legresy et al., 2004). We use tidal currents from the CATS2008 tidal model (Padman et al., 2002) and apply the resultant time varying drag to the base of the ice shelf in the 'RF_currents' experiment, as described in Appendix F. We ran the model with two different drag coefficients, a 'canonical' value of 3×10^{-3} and an 'extreme' value of 3×10^{-2}. Modelled M_{sf} amplitude when using the higher drag coefficient are shown in Fig. 4h. These results reveal that strong tidal currents in combination with high drag coefficients could be locally important, increasing M_{sf} amplitudes in some areas by over 10% compared to the 'default_setup'. Overall, however, the effect of adding this mechanism is far too small to explain observations, even when using an extreme upper-range value for the drag coefficient.

All of the experiments described above use a constant velocity boundary condition along grounding lines. As a consequence, amplitudes of any temporal variations in ice flow go to zero towards the edges of the computational domain. In order to verify that this choice of boundary condition does not significantly affect the tidal response of our model over the main bulk of the ice shelf we conduced a further modelling experiments where the boundaries of the computational domain were placed

further upstream within all the main ice-streams flowing into the the Filchner-Ronne ice shelf. This setup is referred to as the 'RF_streams' setup and is described further in Appendix B. In the RF_streams setup the lateral extent of these additional grounded regions is chosen so that ice velocity along their boundary is approximately zero, while their upstream extent is chosen to be further than any observed tidal effects in the region (i.e. $>100\,\mathrm{km}$). We find that around the grounding lines of major ice streams this leads to an increase the M_{sf} amplitude. However, over the majority of the shelf the differences between the two simulations are generally less than 10% (Fig. 4c). Since including the grounded ice streams greatly increases the computational cost of running the model and we are focusing on replicating GPS observations across the main shelf we use this result to justify not including grounded ice in our domain in all other numerical experiments.

3.2.2 Grounding line migration experiments

None of the numerical experiments described above were able to reproduce the observed Msf amplitudes and despite all our efforts modelled Msf amplitudes are only about 10% of observed values. This suggest that hitherto we may have not included the physical mechanism responsible for generating the observed Msf signal in our model. We stress that we have, however, been able to reproduced the spatial pattern and the amplitudes of the short-periodic (horizontal) tidal modulation in flow, as well as the spatial pattern in the long-periodic tidal modulation.

We now include a physical mechanism that has, until now, been missing from our modelling efforts. This mechanism involves grounding-line migration in response to tides. We use the 'RF_GLmigration' model version to run several experiments that explore the role of this mechanism in generating the pervasive M_{sf} signal observed on the Filchner-Ronne Ice Shelf. Since the amount by which the grounding line will migrate is highly dependant on local bed slopes, of which we have very poor knowledge, we implement this mechanism using the simple analytical approach derived by Tsai and Gudmundsson (2015). In essence, upstream and downstream migration distances are generally expected to be different and can be written as $\Delta L^+ = \Delta S^+/\gamma^+$ and $\Delta L^- = \Delta S^-/\gamma^-$, where L is migration distance and the positive or negative indices indicate positive or negative vertical tidal motion. Two parameters control the distance that the GL migrates up or downstream: γ^+ and γ^-, which determine the upstream and downstream migration distance respectively as a function of local tidal height. A more detailed description of our implementation of this mechanism can be found in Appendix E. With GL migration modelled in this way, the experiments that follow include several effects that could generate an M_{sf} signal: asymmetric grounding line migration, temporal variations in buttressing and periodic narrowing/widening of the ice shelf.

A simulation using $\gamma^+ = 6 \times 10^{-4}$ and $\gamma^- = \gamma^+/7.2$ yields a strong M_{sf} signal with an amplitude of $\sim 0.5\,\mathrm{m}$ near the ice front, matching reasonably well with observations (Fig. 5a). This choice of parameters is equivalent to a maximum upstream migration of 5 km (or $\sim 700\,\mathrm{m}$ downstream) for a positive (or negative) vertical tidal motion of 3 m. The migration is asymmetric (since $\gamma^+ > \gamma^-$) and this degree of asymmetry is within the range that might be expected based on geometric arguments (Tsai and Gudmundsson, 2015). We thus find that this mechanism is capable of producing Msf amplitudes matching observations.

We can explore what happens to the M_{sf} amplitude if just the asymmetric component of the grounding line migration nonlinearity is removed (i.e. $\gamma^+ = \gamma^- = 1.05 \times 10^{-3}$). The resulting M_{sf} amplitude with a symmetric grounding line migration but the same total migration distance over one tidal cycle is shown in Fig. 5c. The M_{sf} amplitude is generally $\sim 50\%$ smaller
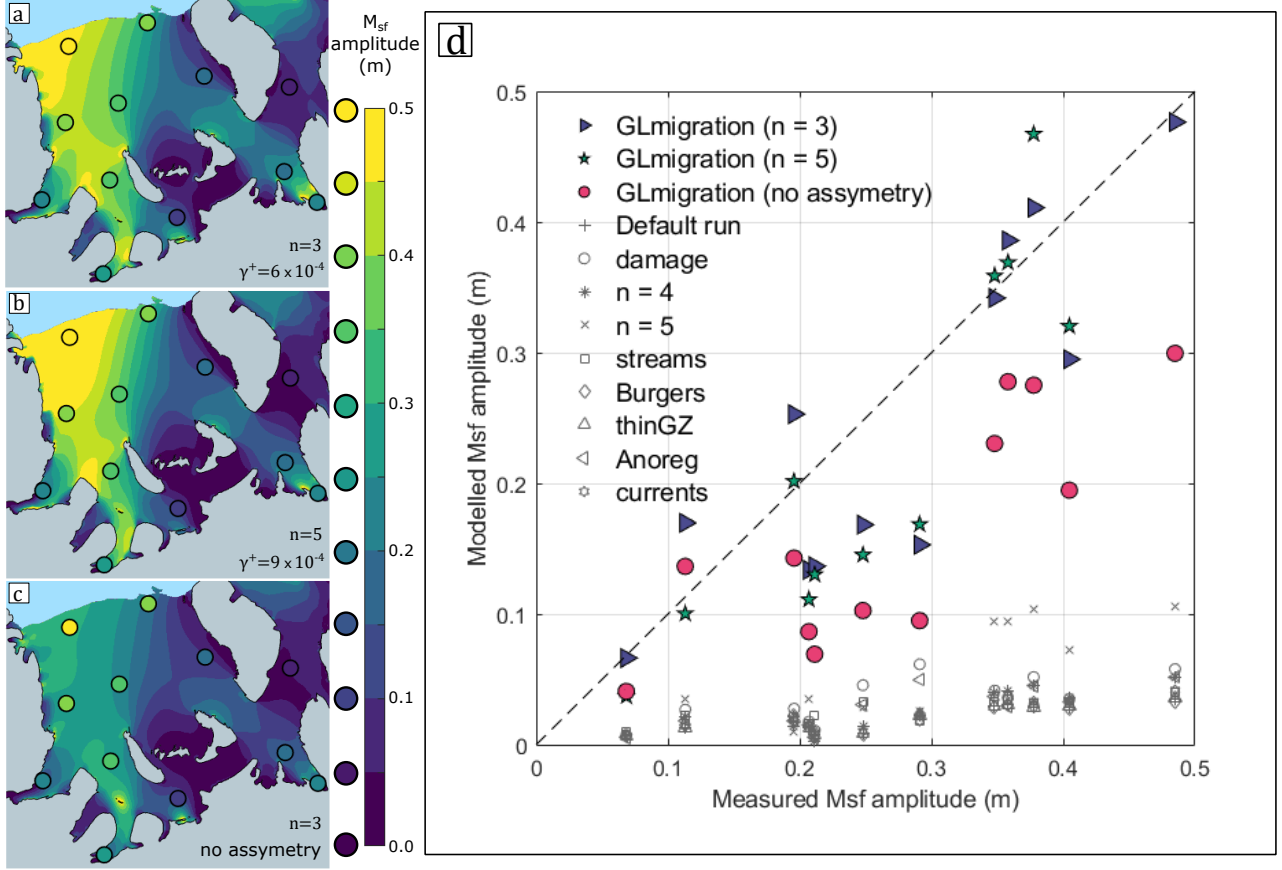
Figure 5. Modelled M_{sf} amplitude on the Ronne Ice Shelf for three variants of the RF_GLmigration model experiment. Panel a uses $n = 3$, $\gamma^+ = 6 \times 10^{-4}$ and $\gamma^- = \gamma^+/7.2$, panel b uses $n = 5$, $\gamma^+ = 9 \times 10^{-4}$ and $\gamma^- = \gamma^+/7.2$ and finally panel c uses $n = 3$ and $\gamma^- = \gamma^+$ (i.e. no asymmetric grounding line migration). Observed M_{sf} amplitude is indicated by the filled circles using the same colour scale. Panel d compares measured and modelled M_{sf} amplitude at each of the marked locations for runs that include the GL migration mechanism (coloured symbols) and those previously presented that do not (grey symbols).

than in the asymmetric case, although still larger than experiments with no GL migration (Fig. 5d), and certain areas such as the Kershaw Ice Rumples (KeIR) generate a strong M_{sf} signal.

We conduct a final experiment in which we combine the GL migration mechanism with an ice rheology in which $n = 5$ in the Glen-Steinemann law. We explore this particular combination because the choice of n was found to have the next largest effect on M_{sf} amplitude (Fig. 4d) and this parameter remains poorly constrained (e.g. Cuffey and Paterson, 2010), yet is of great importance to transient ice sheet behaviour. Increasing the exponent in the flow law leads to a larger M_{sf} signal across the shelf and so we can obtain an equally good match to the observed M_{sf} amplitude with a lower γ^+ of 9×10^{-4} (Fig. 5b).

In this case, upstream and downstream migration distances needed to fit observations are 33% smaller than with a choice of $n = 3$ but qualitatively the spatial pattern of the long-period response is largely unchanged.

4   Discussion

We find that strong modulation of ice-shelf flow at the short-period M_2 frequency is generated by tilting of the ice shelf, supporting the hypothesis of Makinson et al. (2012). This tilt occurs through a combination of phase differences in high tide times around the domain and the lower amplitude vertical tides at the ice shelf front, leading to a rotating tilt vector centered around the M_2 amphidromic point in the Weddell Sea. The modelled amplitude of horizontal ice shelf displacement at M_2 frequency is very similar between all model experiments that used the same elastic rheological parameters and almost completely insensitive to changes in either the viscous ice rheology or the inclusion of other mechanisms such as tidal currents and GL migration. These results demonstrate that the short frequency modulation of ice-shelf flow arises from simple linear elastic processes. Tidal current drag has previously been posited as a possible explanation for the modulation of horizontal ice-shelf flow (Doake et al., 2002; Legresy et al., 2004; Brunt and MacAyeal, 2014), a mechanism which we can now discount for any reasonable choice of drag coefficient.

The modelled M_2 amplitude was only sensitive to our choice for the Young's modulus (E) and a best fit to GPS observations was found using $E = 2.4$ GPa. This Young's modulus can be thought of as an 'effective' value, relevant for tidal periods, since for a viscoelastic material subjected to a periodic forcing the Young's modulus is a function of loading frequency. Linear elastic beam models have often been fitted to measurements of tidal flexure to obtain a wide variety of values for the 'effective' Young's modulus of ice (Lingle et al., 1981; Stephenson, 1984; Kobarg, 1988; Smith, 1991; Vaughan, 1995; Schmeltz et al., 2002; Sykes et al., 2009; Hulbe et al., 2016), however most of these arguably mistakenly treat the resulting E as a material constant and furthermore they are highly sensitive to local factors such as basal crevassing (Rosier et al., 2017b). The horizontal M_2 frequency ice-shelf displacement in our model is generated by strain in the main body of the shelf as it tilts due to differential tidal amplitudes. Therefore, unlike previous studies which rely on very localised measurements, this model provides an excellent opportunity to estimate the viscoelastic properties of ice shelves.

The amplitude of the modelled M_{sf} response was also found to be sensitive to the Young's modulus, since this changes the bending stresses in the grounding zone. On the other hand, the strength of the short period M_2 signal was effectively independent to any changes in viscous ice rheological parameters and indeed almost any other change made to the viscous model parameters. This finding justifies our strategy of first tuning the elastic properties of the model to match observed M_2 response before moving on to exploring the processes and parameters that play a role in generating the M_{sf} signal.

Our study investigates the two mechanisms that have been proposed to explain the generation of the M_{sf} signal across an entire ice shelf: non-linear flexural ice softening and grounding line migration. We test our model results against a comprehensive GPS data sets collected over more than a decade on the Filchern-Ronne ice shelf. This ice shelf is subjected to some of the largest semi-dirunal tides found with up to 8m peak-to-peak amplitudes.

The flexural ice softening mechanism generates an M_{sf} signal as a direct result of the nonlinear rheology of glacial ice. The amplitude of this effect depends on the stress exponent n and to some degree on the spatial variation in the rate factor A.

Tidally induced grounding line migration can be subdivided into several nonlinear effects which will all play a potential role in generating an M_{sf} signal: periodic narrowing and widening of the ice shelf, reduction in basal shear stress, reduced buttress-ing from ice rises/rumples and grounding line asymmetry. With our modelling approach we cannot address the reduction in basal shear stress which will occur as the grounding line migrates upstream on major outlet glaciers, however the other three have been tested using the 'RF_GLmigration' model version (Fig.5).

While the flexural ice softening mechanism is capable of generating an M_{sf} response, we have found that no tested combi-nation of parameters or further model modifications involving visco-elastic rheological laws or model-geometry modifications can produce a sufficiently large amplitude M_{sf} signal to match observations through this mechanism alone (Fig. 4). This mech-anism must be responsible for some of the observed M_{sf} signal, since the nonlinear rheology of ice is well established, but it cannot explain the pervasive and strong M_{sf} signal that is observed over the entire Ronne Ice Shelf.

On the other hand we do find that grounding-line migration can produce large-amplitude fortnightly modulation in ice-shelf flow. Despite the relatively simple implementation employed here, the addition of this process into the model can easily produce an M_{sf} signal that matches observed M_{sf} amplitude and the broad scale spatial distribution (Fig. 5a). It would presumably be possible to obtain an exact fit to observations by allowing the grounding zone geometry to vary spatially, however finding the optimal geometry is a daunting inverse problem beyond the scope of this paper.

Grounding line migration has been suggested as the source of fortnightly modulation in ice-shelf flow in two previous studies; through its effects on ice shelf width (Minchew et al., 2016) or buttressing stresses (Robel et al., 2017). These studies both showed how a horizontal M_{sf} signal could be generated on an ice shelf from a vertical semidiurnal tidal forcing but used a number of simplifying assumptions. Here, we have used a 3D model of the entire region that includes all the stress terms, thus also flexural stresses that are neglected in the two simpler models. This combination of a more complete model and a realistic geometry, together with the numerous remote sensing a in-situ GPS observations, enables us to put tighter constraints on any proposed mechanism. Model parameters that, for example, affect the spatial pattern of secular ice flow (e.g. A and n) also impact the modeled temporal variation in ice flow generated through tidal action. As a consequence, several hitherto potential mechanisms for the generation of long-periodic tidal modulation in ice flow can now be be discounted as viable explanations.

Increasing the exponent n in the ice rheology increases the M_{sf} amplitude, or conversely reduces the distance that the grounding line needs to migrate to match the observed M_{sf} signal by 33%. Without better knowledge of the distance that grounding lines are migrating over the entire ice shelf this result cannot be directly used to estimate viscous ice rheology but obtaining these data is certainly possible (e.g. Schmeltz et al., 2001; Brunt et al., 2011; Milillo et al., 2017). The migration distances we investigate in this modelling study are within the range obtained by satellite estimates; in this region, Brunt et al. (2011) identified areas in which grounding lines were migrating almost 10 km over one tidal cycle.

Several features of the modelled M_{sf} response for the RF_GLmigration experiment deserve specific mentions. Unsurpris-ingly, there is virtually no M_{sf} signal generated in regions where the ice shelf flows slowly, such as behind Berkner Island and Henry Ice Rise. Somewhat more interesting is the lack of an M_{sf} signal in our modelled results along the Eastern coast of the

Ronne Ice Shelf, despite a very large M_{sf} amplitude on the opposite Orville Coast (Fig. 5). This is because the shear margin is located some distance from the grounding line (Fig. 1), meaning that migration of the grounding line is not felt by the main ice shelf (but where the grounding line and shear margin do coincide, at the Southern tip of Berkner Island, an M_{sf} signal is generated). Upon closer inspection, many of the regions that generate a strong M_{sf} signal coincide with areas where the shear margin is close to the grounding line.

Our implementation of tidally-induced grounding line migration is limited in several ways. Most importantly, without accurate knowledge of bed geometry we have had to resort to assuming equal local bed slopes around all grounding lines. In reality, it is likely that in many areas the grounding line migrates only short distances (although conversely we may be underestimating the migration in certain areas). Furthermore, we do not allow the grounding line to migrate in regions of inflow to the ice shelf since our analytical approach would not yield accurate ice velocities across these grounding lines. However, as we are focused on matching the broad scale features of the M_{sf} signal, and localised M_{sf} generation is found to decay over relatively short distances (Fig. 5c), these limitations are not expected to affect our main findings. This second point is further supported by remote sensing observations which show that the M_{sf} signal is spatially heterogeneous (Minchew et al., 2016).

Several previous studies have shown that the nonlinear response to vertical tidal motion which generates the M_{sf} signal also leads to a change in the mean ice velocity (Gudmundsson, 2007, 2011; Rosier et al., 2014; Rosier and Gudmundsson, 2018). Our regional model, that can broadly replicate the M_{sf} signal across the Filchner-Ronne Ice Shelf, now allows us to quantify the magnitude of this effect on an ice shelf for the first time. We ran a repeat of the 'RF_GLmigration' experiment, but with no vertical tidal forcing, and compared the mean velocity in this simulation with that of our best fit to the observed M_{sf} signal. We find that, averaged across the entire ice shelf, ice flow is enhanced by $\sim$21% due to the presence of tides. Much of this tidal flow enhancement is confined to certain portions of the shelf where the local enhancement can be much higher, particularly along the Zumberge and Orville Coasts, i.e. ice flowing out from IIS, RuIS and Evans Ice Stream. This suggests that a potentially important feedback exists between tidal amplitude and ice shelf geometry, i.e. if the ice shelf were to thin or retreat it would alter tides sufficiently to further compound changes in ice flow.

5   Conclusions

We are able to obtain a good agreement between our model and observations of short-periodic tidal modulation in horizontal flow. This study therefore allows us to confirm the previously untested theory of Makinson et al. (2012), that this behaviour arises from the linear elastic response of ice to changes in slope resulting from the relatively high frequency semidiurnal tides. We are also able to replicate, here for the first time, the size and spatial pattern of the observed long-periodic (i.e. longer than a day) horizontal motion of the Filchner-Ronne ice shelf by including a nonlinear mechanism related to grounding-line migration over tidal cycles. As with other nonlinear mechanisms proposed previously, this involves a nonlinear energy transfer from the two main semidiurnal tidal constituents (M_2 and S_2) to the long-periodic M_{sf} tidal constituent.

A nonlinear response to tidal bending stresses has been previously proposed as a possible mechanism to explain observed long-period horizontal motion (Rosier and Gudmundsson, 2018) and in our model this does produce the same general type of

a response. However, our large-scale modeling approach using realistic geometry of the Filchner-Ronne ice shelf shows that the generated long-period amplitude is too small and its spatial pattern inconsistent with observations. We thus arrive at the lateral migration of grounding lines over a tidal cycle as the most promising candidate for explaining the observations of tidal modulation on Filchner-Ronne ice shelf.

5   In our model, the lateral migration of grounding lines gives rise to several different nonlinear mechanisms that all act together. First, the horizontal migration distance is an asymmetrical function of vertical tidal amplitude (this aspect of grounding line migration arises whenever the ice-thickness gradient changes across the grounding line), and this is an example of a *geometrical* nonlinearity. Secondly, ice-shelf flow is a nonlinear function of width and stress for non-Newtonian fluid such as ice. This suggests that observations of tidal modulation of ice-shelf flow can be utilized to extract information about rheology of ice.

10   However, this can only be done if bed geometry and ice thickness across the grounding line are sufficiently well known to calculate the migration distance. Alternatively, if independent observations of lateral migration of grounding lines in response to tides are available, the migration distance can be prescribed directly, in which case the stress exponent (n) can be solved for using a fairly simple modelling approach. Using tidal observations in this manner to extract information about ice rheology is an intriguing possibility that needs to be explored further.

15   *Data availability.* The GPS data set that was analysed to determine horizontal tidal displacement of the Ronne Ice Shelf is publicly available through the UK Polar Data Centre at http://doi.org/10.5285/4fe11286-0e53-4a03-854c-a79a44d1e356 and the analysis of that dataset is carried out in Rosier et al. (2017a).

Appendix A: Inversion for ice rate factor

In order to conduct our 3D tidal model experiments we need to ensure that the model reproduces the observed mean ice flow

20   across the whole computational domain. This we achieve by inverting for the spatial distribution of the rate factor A for any given value of the stress exponent n. Rather than conducting this inversion using our computationally demanding MSC Marc full-Stokes finite element model, we perform this inversion step using the vertically-integrated ice flow model Úa.

The Úa ice-flow model uses the finite element method to solve the shallow shelf (SSA) equations (e.g. Hutter, 1983; MacAyeal, 1989), as described in more detail in (Gudmundsson et al., 2012). The inversion procedure that we use in the

25   Úa model seeks to minimise the misfit between observed and modelled surface velocities by minimising $\log A$, using the adjoint method to calculate the gradient of the cost function as first described for ice flow models by (MacAyeal, 1992, 1993). The cost function being minimised also contains a Tikhonov regularisation term penalising large spatial gradients in $\log A$. For all but one of our simulations we determine the amount of regularisation in our inverted field through an L-curve analysis. We also did experiments without any regularisation ('RF_Anoreg' experiment).

30   Using Úa the inversion procedure was conducted for a much larger domain than that of the full-Stokes model, including the entire drainage basin of the Filchner-Ronne Ice Shelf and for flow exponent values of $n = 3$, $n = 4$ and $n = 5$. The inversion
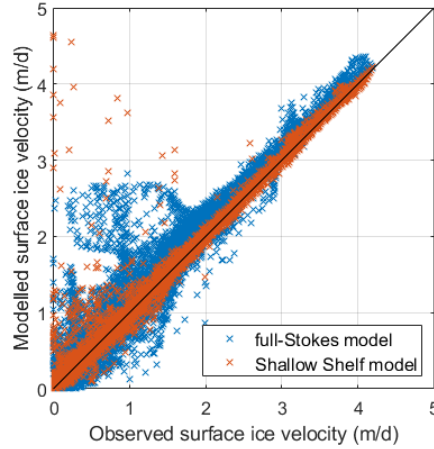
Figure A1. Comparison between observed surface ice velocities, obtained from the MEaSUREs version 2 dataset (Rignot et al., 2017, 2011b; Mouginot et al., 2012), and modelled ice velocities using either the 3D model (Section 2.1, blue crosses) or the Úa model (red crosses).

algorithm was run for several hundred iterations until the change in cost function in each successive step was below some small tolerance value. The mean absolute difference between observed and modelled surface velocities after the completing the inversion (for the $n = 3$ inversion with regularisation) was $18.3\,\mathrm{m\,a^{-1}}$ over the entire domain and $22.5\,\mathrm{m\,a^{-1}}$ across just the ice shelf. Since the assumptions of the SSA, used by Úa, are well met for floating ice shelves we expect that using the resulting
5   inverted fields of A in our full-Stokes 3D model will produce almost an identical ice-flow velocity fields. We did, indeed, find this to be the case, see Fig. A1 showing a comparison between calculated and measured velocity fields as calculated with both the SSA model 'and full-Stokes model MSC Marc using the exact same A distribution.

Appendix B: Modelling of grounded ice

The main challenge to address when adding grounded ice streams into the 'RF_streams' model domain is to reproduce the
10 correct basal sliding velocity (v_b). We use a Weertman sliding law of the form

$$v_b = \beta \tau_b^m \tag{B1}$$

where β is basal slipperiness, τ_b is the basal traction and m is a stress exponent. Using an inverted slipperiness field from a shallow shelf model (as we can do for the rate factor on the ice shelf, see Sec. A) is not possible as the difference in the stress regime between the two models can become large on grounded ice and thus yields a velocity field that does not match
15 observations.

We use the inverse Robin approach outlined in Arthern and Gudmundsson (2010) that consists in solving the forward problem once with standard boundary conditions (denoted $\mathcal{NP}$) and then the slightly modified Dirichlet problem (denoted $\mathcal{DP}$) in which the stress free upper surface condition (Eq. 10) is replaced by a Dirichlet condition where horizontal velocities

derived from observations are imposed. The aim of this procedure is to minimize the Kohn and Vogelius cost function:

$$\mathcal{J}_{kv} = \int\limits_{\Gamma_b} \beta \left| \boldsymbol{v}^N - \boldsymbol{v}^D \right|_F^2 d\Gamma \tag{B2}$$

where $\boldsymbol{v}^N$ and $\boldsymbol{v}^D$ are basal velocities obtained by solving $\mathcal{NP}$ and $\mathcal{DP}$ respectively and $|.|_F^2$ denotes the Frobenius norm. The Gateaux derivative of the cost function $\mathcal{J}_{KV}$ with respect to the A is given by

$$d_\beta \mathcal{J}_{kv} = \int\limits_{\Gamma_b} \beta' \left(\left| \boldsymbol{v}^D \right|_F^2 - \left| \boldsymbol{v}^N \right|_F^2 \right) d\Gamma \tag{B3}$$

This derivative is strictly only exact for a linear ice rheology, nevertheless we use it here as an approximation to the true derivative as has been done by previous authors (Arthern and Gudmundsson, 2010; Gillet-Chaulet et al., 2012).

Following Gillet-Chaulet et al. (2012), we make several modifications to the original approach described by Arthern and Gudmundsson (2010). Firstly we apply a change of variables and invert for $\alpha = \log_{10} \beta$ which avoids any unphysical negative values appearing during the inversion procedure. This necessitates adding a correction to the gradient given in Eq. B3 of

$$d_\alpha \mathcal{J}_{kv} = d_\beta \mathcal{J}_{kv} \ln(10) \beta \tag{B4}$$

Secondly, because both data and model errors are present, it is necessary to avoid over-fitting the model to data which would lead to spurious changes in slipperiness. To this end, we impose a smoothness constraint on the total cost function by adding a Tikhonov style regularisation term of the form

$$\mathcal{J}_{reg} = \frac{\gamma}{2} \int\limits_{\Omega} |\nabla \alpha|^2 dV \tag{B5}$$

where γ is a parameter that must be carefully chosen to ensure a sensibile compromise between a smooth solution and small misfit. We perform an L-curve analysis to determine an optimum value of $\gamma = 10^{-3}$.

In the FEM context this regularisation term can be easily evaluated given the stiffness matrix, $\mathbf{K}$, such that the regularisation term in Eq. B5 is given by

$$\mathcal{J}_{reg} = \frac{\gamma}{2} \alpha^T \mathbf{K} \alpha. \tag{B6}$$

The gradient of this term with respect to α is simply

$$d_\alpha \mathcal{J}_{reg} = \gamma \mathbf{K} \alpha. \tag{B7}$$

Finally, the total cost function we seek to minimise is $\mathcal{J} = \mathcal{J}_{kv} + \mathcal{J}_{reg}$ with gradient $g = d_\alpha \mathcal{J}_{kv} + d_\alpha \mathcal{J}_{reg}$ given by Eqs. B4 and B7.

We use the native minimisation algorithm in MATLAB© to minimise $\mathcal{J}$. Once the inversion procedure has converged to produce a slipperiness field for grounded ice we can use the sliding law in Eq. B1 as a boundary condition for the grounded parts of the model. The same Dirichlet BC that is used on grounded boundary nodes in the 'default setup' (Eq 11) is applied to nodes at the boundaries of the newly added ice streams.

Appendix C: Calculation of a damage field

We employ a continuum damage mechanics approach to simulate the effects of damage on ice behaviour. In this framework, the elastic modulus E is pre-multiplied by a damage factor, D, such that $\tilde{E} = E(1 - D)$ where $\tilde{E}$ is now the effective elastic modulus of damaged ice. The damage factor can be thought of as a measure of the amount of voids in a given unit volume and a high damage factor reduces the portion of a body that can support a load. This simple approach means that in areas of high damage, such as where the ice is heavily crevassed, the effective elastic modulus is reduced and so the ice is less stiff.

We do not allow damage to evolve or advect on the shelf and instead we use the approach of Borstad et al. (2013) to calculate a static damage field. The basic principal of their approach is to take the results of an inversion for the ice rigidity ($B = A^{1/n}$) and assume that spatial variations in this field arise from variations in temperature, back stress and damage. The damage field is then calculated as

$$D = 1 - \frac{B_{i-}}{B(T)}, \tag{C1}$$

where

$$B_{i-} = \begin{cases} B_i & \text{if } B_i \leq B(T) \\ B(T) & \text{otherwise} \end{cases} \tag{C2}$$

and $B(T)$ is the ice rigidity that would be expected based purely on its dependence on temperature.

The only missing ingredient in the equations described above is a temperature field of the ice shelf in order to obtain $B(T)$. We use the analytical solution for ice shelf temperature from Holland and Jenkins (1999) which includes both diffusion and vertical advection. The solution assumes that vertical velocity in the ice shelf is equal to the basal melting rate (w_B) and that the ice shelf is in steady state, such that $w = (\rho_w/\rho)w_B$. In addition, surface and basal temperatures are needed as boundary conditions for the solution. We obtain the surface temperature field T_S as a yearly average of the snow layer temperature from ERA-interim (Dee et al., 2011). We then fix temperature at the base of the ice shelf (T_B) at -2°C. The resulting vertical temperature profile is given by

$$T(z) = \frac{(T_S - T_B)\exp\left(\frac{-wz}{\kappa}\right) + T_B - T_S \exp\left(\frac{wh}{\kappa}\right)}{1 - \exp\left(\frac{wh}{\kappa}\right)}, \tag{C3}$$

where $\kappa = 1.14\text{x}10^{-6}$ is the ice shelf thermal conductivity. With this temperature field, we calculate the temperature dependant ice rigidity using the relation derived in Smith (1981).

The resulting damage field, as calculated from Eq. C1, is shown in Fig. C1. An exhaustive assesment of the resulting damage field is beyond the scope of this study, but areas of high damage are identified along shear margins giving some confidence that this calculation yields a sensible result. The damage factor enters the model by altering the modelled elastic behaviour of ice in regions where damage is high through a reduction in the effective elastic modulus, as outlined above.
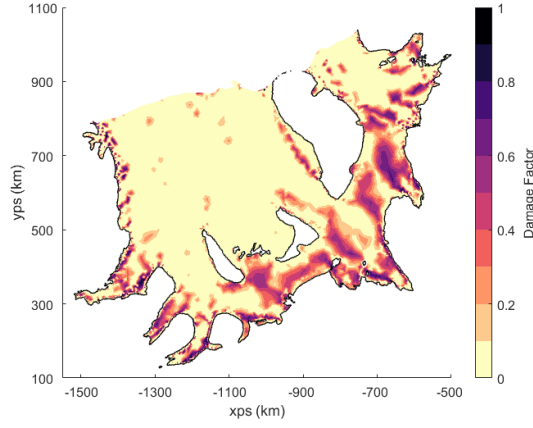
Figure C1. Damage factor field over the Filchner-Ronne Ice Shelf, as calculated with Eq. C1.

Appendix D: Burgers rheology

The viscoelastic rheological model used in the majority of full-Stokes ice-flow model experiments to date is the Maxwell model, consisting of a viscous dashpot and elastic spring connected in series (Sec. 2.1). When a stress is applied to a body of ice this rheological model captures both the instantaneous elastic deformation and the long-term viscous response and is one of the simplest representations of viscoelastic behaviour. Another relatively simple rheological representation is given by a Kelvin model, consisting of a viscous dashpot and elastic spring connected in parallel. In this case the model exhibits a delayed elastic response commonly found in many viscoelastic materials and missed in the Maxwell model. The Kelvin model does not, however, capture either instantaneous elastic deformation or long-term viscous behaviour and thus would be of limited use in this modelling framework. A more complex model is needed to capture all of these behaviours and for that purpose we can use a Burgers model, consisting of a Kelvin and Maxwell element connected in series.

The constituitive equation of the Burgers model for deviatoric behaviour is given by

$$\tau_{ij} + p_1\dot{\tau}_{ij} + p_2\ddot{\tau}_{ij} = q_1\dot{e}_{ij} + q_2\ddot{e}_{ij}, \tag{D1}$$

where

$$p_1 = \frac{\eta_M}{G_M} + \frac{\eta_M}{G_K} + \frac{\eta_K}{G_K}, \tag{D2}$$

$$p_2 = \frac{\eta_K\eta_M}{G_KG_M}, \tag{D3}$$

$$q_1 = 2\eta_M \tag{D4}$$

and

$$q_2 = \frac{2\eta_K\eta_M}{G_K}. \tag{D5}$$

In the equations set out above, η_M and η_K are the viscosities of the Maxwell and Kelvin elements of the Burgers model, while G_M and G_K are the corresponding shear moduli, related to the Young's Modulus and Poisson's ratio through Eq. 5 (Shames

5   and Cozzarelli, 1997). The volumetric deformation is assumed to be elastic and is defined in terms of the bulk modulus K as

$$\sigma_{ii} = 3K\varepsilon_{ii}, \tag{D6}$$

where $K = E/3(1-2\nu)$. The instantaneous elastic response of the Burgers model is determined by the shear Modulus G_M in the Maxwell element and by the bulk modulus K. The Kelvin element parameters, G_K and η_K, determine the delayed elastic response (primary creep). Finally, the steady-state viscous strain which is the only behaviour included in most ice shelf models

10   is determined by the viscosity of the dashpot in the Maxwell element (η_M). Following Gudmundsson (2011) and Reeh et al. (2003), we use the values $G_M = 3.5$GPa, $K = 8.9$GPa, $G_K = 3.3$GPa, $\eta_K = 600$ GPa s and set η_M to the standard viscosity used in Glen's flow law. A major disadvantage of using a Burgers rheology is that, due to the short relaxation time of the Kelvin element (of the order of minutes), the model requires very short time steps to accurately model the primary creep behaviour.

Appendix E: Grounding line migration

15   Calculating tidally induced grounding line migration directly, by solving the contact problem, has been done previously using this model in a 2D flowline case (Rosier et al., 2014). Solving the contact problem for a high resolution model of the entire Filchner-Ronne region would be prohibitively expensive computationally. Furthermore, with no detailed information on the bed slope around (and particularly downstream of) grounding lines this approach would still not yield a reliable assessment of grounding line migration. For these reasons, we reject this methodology and instead we adopt a simpler approach using

20   the analytical solution for grounding line migration proposed by Tsai and Gudmundsson (2015), which gives upstream and downstream migration distances as $\Delta L^+ = \Delta S^+/\gamma^+$ and $\Delta L^- = \Delta S^-/\gamma^-$, where

$$\gamma^+ = \beta + \frac{\rho}{\rho_w}(\alpha - \beta), \tag{E1}$$

$$\gamma^- = \frac{\gamma^+}{(1 - \rho/\rho_w)} \tag{E2}$$

25   and $\Delta S^{+/-}$ is a positive or negative vertical tidal motion. These equations assume hydrostatic equilibrium and constant bed (β) and surface (α) slopes. An important result is that, under these assumptions, the upstream migration distance will be greater than the downstream migration distance for a positive or negative tidal deflection of the same amplitude. This analytical solution agreed reasonably well with GL migration calculated by solving the contact problem in the flowline version of this model (Rosier et al., 2014).
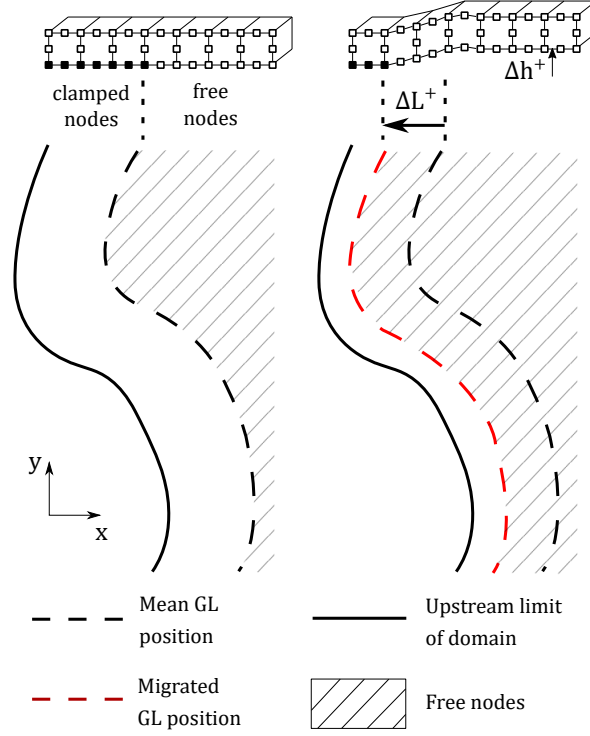
Figure E1. Plan view of a grounding zone, showing how grounding line motion is imposed in the model. Initially the model runs with no tides until it has viscoelastically relaxed. Nodes upstream of the grounding line are clamped at the base and nodes downstream have no constraints. Once tides are switched on, the grounding line can migrate upstream (ΔL^+) or downstream (ΔL^-) and nodes that are outside of the defined grounded area have any constraints removed.

Since, as stated above, we have no accurate knowledge of bed slopes in the model domain we assume that for the purposes of grounding line migration slopes are the same everywhere. This means that the distance the grounding line migrates in the model becomes a function of local tidal amplitude and phase only.

Implementing this into the model involves several steps. Firstly we calculate the distance of every node from the default grounding line position as given by Bedmap2, d_{GL}, where distance is defined as positive for nodes upstream of the grounding line and negative for nodes downstream. Then, given the current local sea surface height, we calculate the current grounding line position using the equations derived by Tsai and Gudmundsson (2015). The basal boundary condition is then applied to nodes along the base of the ice shelf as follows:

$$u, v, w = \begin{cases} 0 & \text{if } d_{GL} \geq \Delta h \\ \text{free} & \text{otherwise} \end{cases} \tag{E3}$$

A weakness of this approach is that it cannot be used in a region where ice is flowing rapidly across the grounding line, i.e. at the outlet of major ice streams, since the basal sliding velocity of grounded nodes is set to zero. Therefore we do not apply this BC in these locations.

A different finite element mesh is needed for any experiments that include GL migration, since the domain must include a band upstream of the GL which it can migrate into. We add a 10 km band of ice everywhere upstream of GLs except those at the outlet of major ice streams. Mesh resolution in this band is ~ 500 m to resolve GL motion as well as possible without creating an excessively large number of additional elements. A schematic showing how grounding line migration is implemented in our finite element model is shown in Fig. E1.

Appendix F: Sub ice shelf currents

In order to simulate the effect of tidal current drag on the ice shelf, we use the depth averaged tidal currents from the CATS2008a model (Padman et al., 2002). This provides amplitude and phase of the U and V components of tidal current transport for each of the four major tidal constituents beneath the shelf (M_2, S_2, O_1 and K_1). Following Robertson et al. (1985); Brunt and MacAyeal (2014), the x and y components of basal shear stress (τ_x and τ_y, respectively) resulting from tidal currents are defined as

$$\tau_x = \frac{C_D \rho_w U \left| U_T \right|}{H^2}, \qquad\qquad \tau_y = \frac{C_D \rho_w V \left| U_T \right|}{H^2} \qquad\qquad \text{(F1)}$$

where H is water column thickness, C_D is the drag coefficient and $U_T = \sqrt{U^2 + V^2}$ is the magnitude of the tidal current transport vector. The drag coefficient is an unknown related to the roughness of the ice shelf base. We investigated two choices for C_D, a typical value of 0.003 (Robertson et al., 1985; Brunt and MacAyeal, 2014) and a much higher value of 0.03 which we use to test a theoretical upper limit on tidal current effects. The basal shear stresses are applied directly the bottom face of the ice shelf elements at the same time as vertical tides are initiated within the model.

Appendix G: Temperature effects

The effects of temperature on ice rheology are, to a certain extent, included in every version of the model; since a part of the spatial variation in the inverted rate factor field is caused by temperature. One aspect of temperature variations that is not included however is the change in temperature with depth. This will result in ice that deforms more easily at the base than at the surface, since ice will generally be cooler at the surface and warmer at the ice shelf base. This could conceivable play an important role in the response of an ice shelf to tides and is particularly relevant for the tidal flexure mechanism since here it is the ice rheology that is the source of nonlinearity that we seek to reproduce.

We are specifically interested in the effects of depth variation in ice softness and to explore this in the simplest way possible we assume that, everywhere in the ice shelf, temperature varies linearly from -20°C at the surface to -2°C at the base. We then make the rate factor a function of temperature using the relation derived by Smith (1981).

Appendix H: Thin grounding zone experiment

Ice thickness within the grounding zone (GZ) is modified in the 'RF_thinGZ' experiment to explore how this might affect generation of the M_{sf} signal, in particular by changing flexural stresses resulting from tidal bending. The crude approach that we take for a first order estimate of this affect is to multiply ice thickness h by a factor $1 - \lambda$ that is a function of distance from the grounding line (d_{GL}), defined such that at the grounding line and far away from the grounding zone $\lambda = 0$ but within the grounding zone $0 < \lambda < 1$. The arbitrary function that we choose for this purpose is a log-normal distribution centered around $d_{GL} = $1km, where it reaches a maximum value of 0.1, i.e. leading a maximum reduction in ice thickness of 10%. Multiplying ice thickness by this factor yields a new ice thickness field that retains its overall shape and the effect is confined such that $\lambda \approx 1 \times 10^{-2}$ at $d_{GL} = $10 km and $\lambda \approx 1 \times 10^{-3}$ at $d_{GL} = $20 km (beyond this distance from the grounding line we do not alter ice thickness).

Acknowledgements. We are very grateful to Andrew Bell for his invaluable help with MSC Marc. Sebastian H. R. Rosier was funded by the UK Natural Environment Research Council large grant "Ice shelves in a warming world: Filchner Ice Shelf System" (NE/L013770/1).

References

Alley, S. A. R. B.: Tidal forcing of basal seismicity of ice stream C, West Antarctica, observed far inland, J.Geophys. Res., 102, 15,813–15,196, https://doi.org/10.1029/97JB01073, 1997.

Anandakrishnan, S., Voigt, D. E., and Alley, R. B.: Ice stream D flow speed is strongly modulated by the tide beneath the Ross Ice Shelf, Geophys. Res. Lett., 30, 1361, https://doi.org/DOI: 10.1029/2002GL016329, 2003.

Arthern, R. J. and Gudmundsson, G. H.: Initialization of ice-sheet forecasts viewed as an inverse Robin problem, Journal of Glaciology, 56, 527–533, https://doi.org/10.3189/002214310792447699, 2010.

Bindschadler, R. A., King, M. A., Alley, R. B., Anandakrishnan, S., and Padman, L.: Tidally controlled stick-slip discharge of a West Antasrctic ice stream, Science, 301, 1087–1089, https://doi.org/10.1126/science.1087231, 2003.

Borstad, C. P., Rignot, E., Mouginot, J., and Schodlok, M. P.: Creep deformation and buttressing capacity of damaged ice shelves: theory and application to Larsen C ice shelf, The Cryosphere, 7, 1931–1947, https://doi.org/10.5194/tc-7-1931-2013, 2013.

Brunt, K. M. and MacAyeal, D. R.: Tidal modulation of ice-shelf flow: a viscous model of the Ross Ice Shelf, Journal of Glaciology, 60, 500–508, https://doi.org/https://doi.org/10.3189/2014JoG13J203, 2014.

Brunt, K. M., King, M. A., Fricker, H. A., and Macayeal, D. R.: Flow of the Ross Ice Shelf , Antarctica , is modulated by the ocean tide, Journal of Glaciology, 56, 2005–2009, 2010.

Brunt, K. M., Fricker, H. A., and Padman, L.: Analysis of ice plains of the Filchner-Ronne Ice Shelf, Antarctica, using ICESat laser altimetry, Journal of Glaciology, 57, 965–975, n/a, 2011.

Codiga, D. L.: Unified Tidal Analysis and Prediction Using the UTide Matlab Functions, Tech. rep., Graduate School of Oceanography, University of Rhode Island, Narragansett, RI., 2011.

Cuffey, K. M. and Paterson, W. S. B.: The physics of glaciers 4th ed., Elsevier, Amsterdam, 2010.

De Angelis, H. and Skvarca, P.: Glacier Surge After Ice Shelf Collapse, 299, 1560–1562, https://doi.org/10.1126/science.1077987, 2003.

Dee, D. P., Uppala, S. M., Simmons, A. J., Berrisford, P., Poli, P., Kobayashi, S., Andrae, U., Balmaseda, M. A., Balsamo, G., Bauer, P., Bechtold, P., Beljaars, A. C. M., van de Berg, L., Bidlot, J., Bormann, N., Delsol, C., Dragani, R., Fuentes, M., Geer, A. J., Haimberger, L., Healy, S. B., Hersbach, H., Hólm, E. V., Isaksen, L., Kållberg, P., Köhler, M., Matricardi, M., McNally, A. P., Monge-Sanz, B. M., Morcrette, J.-J., Park, B.-K., Peubey, C., de Rosnay, P., Tavolato, C., Thépaut, J.-N., and Vitart, F.: The ERA-Interim reanalysis: configuration and performance of the data assimilation system, Quarterly Journal of the Royal Meteorological Society, 137, 553–597, https://doi.org/10.1002/qj.828, 2011.

Doake, C., Corr, H. F. J., Nicholls, K. W., Gaffikin, A., Jenkins, A., Bertiger, W. I., and King, M. A.: Tide-induced lateral movement of Brunt Ice Shelf , Antarctica, Geophysical Research Letters, 29, 1–4, https://doi.org/10.1029/2001GL014606, 2002.

Engwirda, D.: Locally-optimal Delaunay-refinement and optimisation-based mesh generation, Ph.D. thesis, School of Mathematics and Statistics, University of Sydney, 2014.

Fretwell, P., Pritchard, H. D., Vaughan, D. G., Bamber, J. L., Barrand, N. E., Bell, R., Bianchi, C., Bingham, R. G., Blankenship, D. D., Casassa, G., Catania, G., Callens, D., Conway, H., Cook, A. J., Corr, H. F. J., Damaske, D., Damm, V., Ferraccioli, F., Forsberg, R., Fujita, S., Gim, Y., Gogineni, P., Griggs, J. A., Hindmarsh, R. C. A., Holmlund, P., Holt, J. W., Jacobel, R. W., Jenkins, A., Jokat, W., Jordan, T., King, E. C., Kohler, J., Krabill, W., Riger-Kusk, M., Langley, K. A., Leitchenkov, G., Leuschen, C., Luyendyk, B. P., Matsuoka, K., Mouginot, J., Nitsche, F. O., Nogi, Y., Nost, O. A., Popov, S. V., Rignot, E., Rippin, D. M., Rivera, A., Roberts, J., Ross, N., Siegert, M. J., Smith, A. M., Steinhage, D., Studinger, M., Sun, B., Tinto, B. K., Welch, B. C., Wilson, D., Young, D. A., Xiangbin, C., and Zirizzotti,

A.: Bedmap2: improved ice bed, surface and thickness datasets for Antarctica, The Cryosphere, 7, 375–393, https://doi.org/10.5194/tc-7-375-2013, 2013.

Furst, J. J., Durand, G., Gillet-Chaullet, F., Tavard, L., Rankl, M., Braun, M., and Gagliardini, O.: The safety band of Antarctic ice shelves, Nature climate change, 6, 479–482, https://doi.org/10.1038/nclimate2912, 2018.

5   Gillet-Chaulet, F., Gagliardini, O., Seddik, H., Nodet, M., Durand, G., Ritz, C., Zwinger, T., Greve, R., and Vaughan, D. G.: Greenland ice sheet contribution to sea-level rise from a new-generation ice-sheet model, The Cryosphere, 6, 1561–1576, https://doi.org/10.5194/tc-6-1561-2012, 2012.

Gudmundsson, G. H.: Fortnightly variations in the flow velocity of Rutford Ice Stream, West Antarctica., Nature, 444, 1063–4, https://doi.org/doi:10.1038/nature05430, 2006.

10   Gudmundsson, G. H.: Tides and the flow of Rutford Ice Stream, West Antarctica, J. Geophys. Res., 112, F04 007, https://doi.org/10.1029/2006JF000731, 2007.

Gudmundsson, G. H.: Ice-stream response to ocean tides and the form of the basal sliding law, The Cryosphere, 5, 259–270, https://doi.org/10.5194/tc-5-259-2011, 2011.

Gudmundsson, G. H.: Ice-shelf buttressing and the stability of marine ice sheets, The Cryosphere, 7, 647–655, https://doi.org/10.5194/tc-7-647-2013, 2013.

15   Gudmundsson, G. H., Krug, J., Durand, G., Favier, L., and Gagliardini, O.: The stability of grounding lines on retrograde slopes, The Cryosphere, 6, 1497–1505, https://doi.org/10.5194/tc-6-1497-2012, https://www.the-cryosphere.net/6/1497/2012/, 2012.

Gudmundsson, G. H., De Rydt, J., and Nagler, T.: Five decades of strong temporal variability in the flow of Brunt Ice Shelf, Antarctica, Journal of Glaciology, 63, 164–175, https://doi.org/10.1017/jog.2016.132, 2017.

20   Haseloff, M. and Sergienko, O. V.: The effect of buttressing on grounding line dynamics, Journal of Glaciology, 64, 417–431, https://doi.org/10.1017/jog.2018.30, 2018.

Holland, D. M. and Jenkins, A.: Modeling Thermodynamic Ice–Ocean Interactions at the Base of an Ice Shelf, Journal of Physical Oceanography, 29, 1787–1800, https://doi.org/10.1175/1520-0485, 1999.

Hughes, T.: Is the west Antarctic Ice Sheet disintegrating?, Journal of Geophysical Research, 78, 7884–7910, 25   https://doi.org/10.1029/JC078i033p07884, 1973.

Hulbe, C. L., Klinger, M., Masterson, M., Catania, G., Cruikshank, K., and Bugni, A.: Tidal bending and strand cracks at the Kamb Ice Stream grounding line, West Antarctica, Journal of Glaciology, 62, 816–824, https://doi.org/10.1017/jog.2016.74, 2016.

Hutter, K.: Theoretical Glaciology: Material Science of Ice and the Mechanics of Glaciers and Ice Sheets, Mathematical Approaches to Geophysics, Springer, 1983.

30   Jellinek, H. H. G. and Brill, R.: Viscoelastic Properties of Ice, Journal of Applied Physics, 27, 1198–1209, https://doi.org/10.1063/1.1722231, 1956.

King, M. A., Makinson, K., and Gudmundsson, G. H.: Nonlinear interaction between ocean tides and the Larsen C Ice Shelf system, Geophysical Research Letters, 38, 1–5, https://doi.org/10.1029/2011GL046680, 2011.

Kobarg, W.: The tide-dependent dynamics of the Ekström Ice Shelf, Antarctica, Berichte zur Polarforschung, Alfred-Wegener-Inst. für Polar-35   u. Meeresforsch., 1988.

Legresy, B., Wendt, A., Tabacco, I., Remy, F., and Dietrich, R.: Influence of tides and tidal current on Mertz Glacier, Antarctica, Journal of Glaciology, 50, 427–435, https://doi.org/10.3189/172756504781829828, 2004.

Lingle, C. S., Hughes, T. J., and Kollmeyer, R. C.: Tidal flexure of Jakobshavns Glacier, west Greenland, Journal of Geophysical Research: Solid Earth, 86, 3960–3968, https://doi.org/10.1029/JB086iB05p03960, 1981.

MacAyeal, D. R.: Large-scale ice flow over a viscous basal sediment: Theory and application to ice stream B, Antarctica, Journal of Geophysical Research: Solid Earth, 94, 4071–4087, https://doi.org/10.1029/JB094iB04p04071, 1989.

5 MacAyeal, D. R.: The basal stress distribution of Ice Stream E, Antarctica, inferred by control methods, Journal of Geophysical Research: Solid Earth, 97, 595–603, https://doi.org/10.1029/91JB02454, 1992.

MacAyeal, D. R.: A tutorial on the use of control methods in ice-sheet modeling, Journal of Glaciology, 39, 91–98, https://doi.org/10.3189/S0022143000015744, 1993.

Makinson, K., King, M. A., Nicholls, K. W., and Gudmundsson, G. H.: Diurnal and semidiurnal tide-induced lateral movement of Ronne Ice
10 Shelf, Antarctica, Geophysical Research Letters, 39, https://doi.org/10.1029/2012GL051636, 2012.

Marsh, O. J., Rack, W., Floricioiu, D., Golledge, N. R., and Lawson, W.: Tidally induced velocity variations of the Beardmore Glacier, Antarctica, and their representation in satellite measurements of ice velocity, The Cryosphere, 7, 1375–1384, https://doi.org/10.5194/tc-7-1375-2013, 2013.

Millillo, P., Rignot, E., Mouginot, J., Scheuchl, B., Morlighem, M., Li, X., and Salzer, J. T.: On the Short-term Grounding Zone Dynamics of
15 Pine Island Glacier, West Antarctica, Observed With COSMO-SkyMed Interferometric Data, Geophysical Research Letters, 44, 10,436–10,444, https://doi.org/10.1002/2017GL074320, 2017.

Minchew, B. M., Simons, M., Riel, B., and Millillo, P.: Tidally induced variations in vertical and horizontal motion on Rutford Ice Stream, West Antarctica, inferred from remotely sensed observations, Journal of Geophysical Research: Earth Surface, pp. 1–24, https://doi.org/10.1002/2016JF003971, 2016.

20 Mouginot, J., Scheuchl, B., and Rignot, E.: Mapping of Ice Motion in Antarctica Using Synthetic-Aperture Radar Data, Remote Sensing, 4, 2753–2767, https://doi.org/10.3390/rs4092753, 2012.

MSC: Marc 2017 Volume A: Theory and user information, MSC MARC, MSC Software Corporation, 2 MacArther Place, Santa Ana, CA 92707, 2017.

Padman, L., Fricker, H. A., Coleman, R., Howard, S., and Erofeeva, S. Y.: A new tide model for the Antarctic ice shelves and seas, Ann.
25 Glaciol., 34, 247–254, 2002.

Pegler, S. S.: Marine ice sheet dynamics: the impacts of ice-shelf buttressing, Journal of Fluid Mechanics, 857, 605–647, https://doi.org/10.1017/jfm.2018.741, 2018.

Pirli, M., Hainzl, S., Schweitzer, J., Köhler, A., and Dahm, T.: Localised thickening and grounding of an Antarctic ice shelf from tidal triggering and sizing of cryoseismicity, Earth and Planetary Science Letters, 503, 78 – 87,
30 https://doi.org/https://doi.org/10.1016/j.epsl.2018.09.024, 2018.

Rack, W., King, M. A., Marsh, O. J., Wild, C. T., and Floricioiu, D.: Analysis of ice shelf flexure and its InSAR representation in the grounding zone of the southern McMurdo Ice Shelf, The Cryosphere, 11, 2481–2490, https://doi.org/10.5194/tc-11-2481-2017, 2017.

Reeh, N., Christensen, E. L., Mayer, C., and Olesen, O. B.: Tidal bending of glaciers: a linear viscoelastic approach, Ann. Glaciol., 37, 83–89, https://doi.org/10.3189/172756403781815663, 2003.

35 Reese, R., Gudmundsson, G. H., Levermann, A., and Winkelmann, R.: The far reach of ice-shelf thinning in Antarctica, Nature climate change, 8, 53–57, https://doi.org/10.1038/s41558-017-0020-x, 2018.

Riedel, B., Nixdorf, U., Heinert, M., Eckstaller, A., and Mayer, C.: The response of the Ekstromisen (Antarctica) grounding zone to tidal forcing, Annals of Glaciology, 29, 239–242, https://doi.org/10.3189/172756499781821247, 1999.

Rignot, E., Casassa, G., Gogineni, P., Krabill, W., Rivera, A., and Thomas, R.: Accelerated ice discharge from the Antarctic Peninsula following the collapse of Larsen B ice shelf, Geophysical Research Letters, 31, https://doi.org/10.1029/2004GL020697, 2004.

Rignot, E., Mouginot, J., and Scheuchl, B.: Ice Flow of the Antarctic Ice Sheet, Science, 333, 1427–1430, https://doi.org/10.1126/science.1208336, 2011a.

5 Rignot, E., Mouginot, J., and Scheuchl, B.: MEaSUREs InSAR-Based Antarctica Ice Velocity Map, Version 2, https://doi.org/https://doi.org/10.5067/D7GK8F5J8M8R, 2017.

Rignot, E. J., Mouginot, J., and Scheuchl, B.: Antarctic grounding line mapping from differential satellite radar interferometry, Geophysical Research Letters, 38, https://doi.org/10.1029/2011GL047109, l10504, 2011b.

Robel, A. A., Tsai, V. C., Minchew, B., and Simons, M.: Tidal modulation of ice shelf buttressing stresses, Annals of Glaciology, 58, 12–20,

10 https://doi.org/10.1017/aog.2017.22, 2017.

Robertson, R., Padman, L., and Egbert, G. D.: Tides in the Weddell Sea, pp. 341–369, American Geophysical Union (AGU), https://doi.org/10.1029/AR075p0341, 1985.

Rosier, S. H. R. and Gudmundsson, G. H.: Tidal bending of ice shelves as a mechanism for large-scale temporal variations in ice flow, The Cryosphere, 12, 1699–1713, https://doi.org/10.5194/tc-12-1699-2018, 2018.

15 Rosier, S. H. R., Gudmundsson, G. H., and Green, J. A. M.: Insights into ice stream dynamics through modeling their response to tidal forcing, The Cryosphere, 8, 1763–1775, https://doi.org/10.5194/tc-8-1763-2014, 2014.

Rosier, S. H. R., Gudmundsson, G. H., and Green, J. A. M.: Temporal variations in the flow of a large Antarctic ice-stream controlled by tidally induced changes in the subglacial water system, The Cryosphere Discussions, 9, 1–33, https://doi.org/10.5194/tcd-9-1-2015, 2015.

Rosier, S. H. R., Gudmundsson, G. H., King, M. A., Nicholls, K. W., Makinson, K., and Corr, H. F. J.: Strong tidal variations

20 in ice flow observed across the entire Ronne Ice Shelf and adjoining ice streams, Earth System Science Data Discussions, 70, https://doi.org/10.5194/essd-2017-70, 2017a.

Rosier, S. H. R., Marsh, O. J., Rack, W., Gudmundsson, G. H., Wild, C. T., and Ryan, M.: On the interpretation of ice-shelf flexure measurements, Journal of Glaciology, 63, 783–791, https://doi.org/10.1017/jog.2017.44, 2017b.

Rott, H., Rack, W., Skvarca, P., and Angelis, H. D.: Northern Larsen Ice Shelf, Antarctica: further retreat after collapse, Annals of Glaciology,

25 34, 277–282, https://doi.org/10.3189/172756402781817716, 2002.

Schmeltz, M., Rignot, E., and MacAyeal, D. R.: Ephemeral grounding as a signal of ice-shelf change, Journal of Glaciology, 47, 71–77, https://doi.org/10.3189/172756501781832502, 2001.

Schmeltz, M., Rignot, E. J., and MacAyeal, D.: Tidal flexure along ice-sheet margins: comparison of InSAR with an elastic-plate model, Annals of Glaciology, 34, 202–208, https://doi.org/doi:10.3189/172756402781818049, 2002.

30 Shames, I. H. and Cozzarelli, F. A.: Elastic and Inelastic Stress Analysis, Taylor and Francis, 325 CHestnut St., Philadelphia, 19106, 1997.

Smith, A. M.: The use of tiltmeters to study the dynamics of Antarctic ice-shelf grounding lines, J. Glaciol., 37, 51–58, 1991.

Smith, G. D.: Viscous relations for the steady creep of polycrystalline ice, Cold regions Science and Technology, 5, 141–150, 1981.

Stephenson, S. N.: Glacier flexure and the position of grounding lines: Measurements by tiltmeter on Rutford Ice Stream Antarctica, Ann. Glaciol., 5, 165–169, 1984.

35 Sykes, H. J., Murray, T., and Luckman, A.: The location of the grounding zone of Evans Ice Stream, Antarctica, investigated using SAR interferometry and modelling, Annals of Glaciology, 50, 35–40, https://doi.org/doi:10.3189/172756409789624292, 2009.

Thomas, R. H.: The Creep of Ice Shelves: Interpretation of Observed Behaviour, Journal of Glaciology, 12, 55–70, https://doi.org/10.3189/S002214300002270X, 1973.

Thompson, J., Simons, M., and Tsai, V. C.: Modeling the elastic transmission of tidal stresses to great distances inland in channelized ice streams, The Cryosphere Discussions, 8, 2119–2177, https://doi.org/10.5194/tc-8-2007-2014, 2014.

Tsai, V. C. and Gudmundsson, G. H.: An improved model for tidally-modulated grounding line migration, Journal of Glaciology, 61, 216–222, https://doi.org/10.3189/2015JoG14J152, 2015.

5 Vaughan, D. G.: Tidal flexure at ice shelf margins, J. Geophys. Res., 100, 6213–6224, 1995.